Energy and Level Width of $^{5}_{2}\mathrm{He}(J^{\pi}=3/2^{-})$ System

Hla Hla Win[1], Aye Myat Wai[2], Bawk La[3] and Lae Lae Win Shwe[4]

Abstract

The purpose of this research is to investigate the energy and level width of $^{5}_{2}\mathrm{He}(J^{\pi}=3/2^{-})$ system. The Gaussian basis wave function is used to solve the two body Schrödinger equation with spin-orbit coupling. The calculated resonance energy and level width is compared with the experimental data and the results are consistent with the experimental data.

Key words: resonance energy, complex scaling method, spin-orbit coupling

Introduction

The nuclear structure is roughly homogeneous distribution of neutrons and protons. $^{5}_{2}\mathrm{He}$ system contains two protons and three neutrons. In this work, $^{5}_{2}\mathrm{He}$ system is assumed as alpha-neutron two body system. The (α-n) system has rather broad resonances but no bound state. The resonance states are solved by using the complex scaling method.

A resonance energy is $E_{res}=E_{r}-i\frac{\Gamma}{2}$ has a negative imaginary part, which is called resonance width. The use of a complex energy allows a classification of the energy levels of a quantum system.

Under complex rotation, the resonance for which $\tan\theta>\frac{k_{I}}{k_{R}}$ are separated from continuum, and the rotated continuum spectra starting from different threshold energies are separately obtained on different 2θ-lines as shown in Fig. 1.

1 Dr, Associate Professor, Department of Physics, Banmaw University
2 Dr, Lecturer, Department of Physics, Banmaw University
3 Lecturer, Department of Physics, Banmaw University
4 Dr, Lecturer, Department of Physics, Yadanarbon University

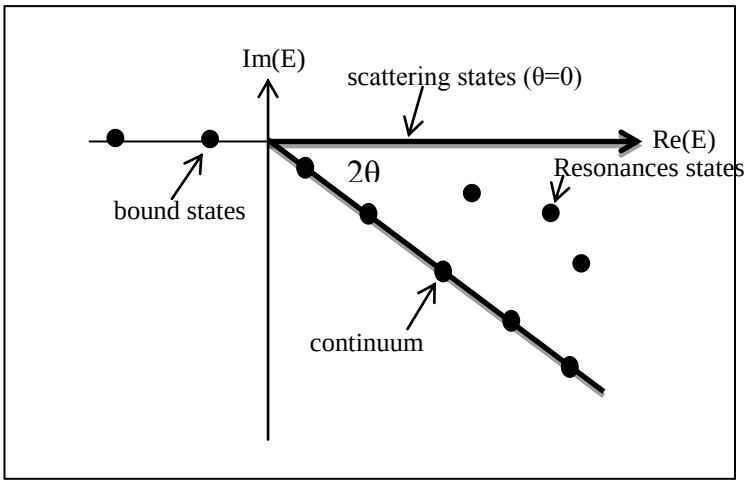

Fig. 1. A schematic distribution of the eigenvalues of the bound states and resonance states.

Complex Coordinate Rotation Method

The method of complex coordinate rotation is used to investigate the resonance states. Thus complex resonance energy is written as

$$E_{res} = E_R - i\frac{\Gamma}{2} \tag{1}$$

where E_R is energy level and Γ is the level width. In the asymptotic region, the resonance wave function is described by purely out going radial part as

$$\Psi(r) \xrightarrow[r\to\infty]{} e^{iKr} \tag{2}$$

where the wave vector $K = K_R - iK_I$ ($K_R \rangle 0$ and $K_I \rangle 0$) and satisfies

$$E = \frac{\hbar^2 K^2}{2\mu} \cdot$$

Thus
$$\Psi(r) \xrightarrow[r\to\infty]{} e^{i(K_R - K_I)r} = e^{iK_R r} e^{K_I r}$$

$$= e^{K_I r}\{\cos(K_R r) + i\sin(K_R r)\} \tag{3}$$

which shows that the asymptotic radial part is oscillating between exponentially growing amplitudes of $e^{K_I r}$.

According to complex rotation method, the following transformation

$$r \rightarrow re^{i\theta} \tag{4}$$

where θ is a rotation angle. The complex scaling operator $\hat{U}(\theta)$ acting on a single particle wave function is defined as

$$\Psi(r) \rightarrow \Psi(re^{i\theta}) = \Psi_\theta(r) = \hat{U}(\theta)\,\Psi(r) \tag{5}$$

Let us see the transformed Schrödinger equation under complex rotation,

$$H(r)\,\Psi(r) = E\,\Psi(r) \tag{6}$$

$$H(re^{i\theta})\Psi(re^{i\theta}) = E\Psi(re^{i\theta}) \tag{7}$$

$$H(re^{i\theta})\,\hat{U}(\theta)\Psi(r) = E\,\hat{U}(\theta)\Psi(r)$$

$$\hat{U}^{-1}(\theta)H(re^{i\theta})\,\hat{U}(\theta)\Psi(r) = E\,\hat{U}^{-1}(\theta)\hat{U}(\theta)\Psi(r)$$

$$\hat{U}^{-1}(\theta)H(re^{i\theta})\,\hat{U}(\theta)\Psi(r) = E\,\Psi(r) \tag{8}$$

By comparing Eq.(6) and (8)

$$H(r) = \hat{U}^{-1}(\theta)H(re^{i\theta})\,\hat{U}(\theta)$$

$$\text{(or)}\quad \hat{U}^{-1}(\theta)H(r)\hat{U}^{-1}(\theta) = H(re^{i\theta}) = H_{\theta}(r) \tag{9}$$

Under this transformation, the energy eigenvalue remains unchanged

$$H_{\theta}(r)\Psi_{\theta}(r) = E\Psi_{\theta}(r)$$

Then the asymptotic resonance wave function is transformed as

$$\Psi_{\theta}(r) \xrightarrow[r\to\infty]{} e^{i(K_R - iK_I)re^{i\theta}}$$

$$\xrightarrow[r\to\infty]{} e^{-(K_R\sin\theta - K_I\cos\theta)r}\, e^{i(K_R\cos\theta + K_I\sin\theta)r} \tag{10}$$

and oscillating with amplitude $e^{-(K_R\sin\theta - K_I\cos\theta)r}$. From the above equation, if $K_R\sin\theta > K_I\cos\theta$ (or) $\tan\theta > \frac{K_I}{K_R}$, the resonance wave functions becomes convergent at the asymptotic region.

According to the relation of the complex resonance energy and wave vector,

$$E_R - iE_I = \frac{\hbar^2}{2\mu}(K_R - iK_I)^2 \tag{11}$$

If $E_R >> E_I$ ($K_R >> K_I$), the boundary condition for resonance state can be expressed as

$$\tan\theta > \frac{K_I}{K_R} \sim \frac{E_I}{2E_R}$$

The rotation parameter θ has an upper limit, $\theta_c = \frac{\pi}{4}$. The Gaussian basis wave functions are transformed under complex rotation.

By introducing r′ as $r' = re^{i\theta}$ (12)

$$r = r'e^{-i\theta} \tag{13}$$

Eq. (7) is written as $H(re^{i\theta})\,\Psi(re^{i\theta}) = E\,\Psi(re^{i\theta})$

$$H(r')\,\Psi(r') = E\,\Psi(r') \tag{14}$$

The transformed Gaussian basis wave function is

$$\Psi_{\theta}(r) = \sum_j c_j(\theta) e^{-\left(\frac{r}{b_j}\right)^2} \quad (15)$$

(or)
$$\Psi(r') = \sum_j c_j(\theta) e^{-\left(\frac{r'}{b_j e^{i\theta}}\right)^2} \quad (16)$$

Eq. (14) becomes

$$H(r') \sum_j c_j(\theta) e^{-\left(\frac{r'}{b_j e^{i\theta}}\right)^2} = E \sum_j c_j(\theta) e^{-\left(\frac{r'}{b_j e^{i\theta}}\right)^2} \quad (17)$$

$$H(r) \sum_j c_j(\theta) e^{-\left(\frac{r}{b_j e^{i\theta}}\right)^2} = E \sum_j c_j(\theta) e^{-\left(\frac{r}{b_j e^{i\theta}}\right)^2} \quad (18)$$

We have to solve the Schrödinger equation which is the same as bound state system except the range parameter b_j becomes $b_j e^{i\theta}$. By diagonalization the Hamiltonian matrix elements, we obtained the complex energy eigenvalues.

Interaction between Alpha and Neutron

The α-n potentials is introduced by Kanada *et al*., (Kanada, 1979) are described. The α-n potential is expressed in the following Gaussian form,

$$V_{\alpha\text{-}n}(r) = \sum_i^{i_{max}} V_i e^{-\beta_i r^2} + \sum_i^{i'_{max}} (-)^{\ell} V_i^{p} e^{-\beta_i^{p} r^2} + \left[\sum_i^{i''_{max}} V_i^{\ell.s} e^{-\gamma_i r^2} + i \sum_i^{i'''_{max}} (-)^{\ell} V_i^{\ell s.p} e^{-\gamma_i^{p} r^2} \right] \vec{\ell}.\vec{s}_N \quad (19)$$

where ℓ is the relative angular momentum between α and neutron, and $\vec{s}_N$ is the spin of neutron. The spin orbit $\vec{\ell}.\vec{s}$ coupling is calculated by using the following equation;

$$\vec{\ell}.\vec{s} = \frac{j(j+1) - \ell(\ell+1) - s(s+1)}{2} \quad (20)$$

The potential strengths and the range parameters are described in Table 1.

Table 1. The size parameters (fm^{-2}) and strength parameters (MeV) of α-n interaction

i	1	2	3
β_i	0.36	0.90	-
β_i^p	0.20	0.53	2.5
γ_i	0.396	0.52	2.2
γ_i^p	0.396	2.2	-
V_i	-96.3	77.0	-
V_i^p	34.0	-85.0	51.0
V_i^{ls}	-20.0	-16.8	20.0
$V_i^{ls,p}$	6.0	-6.0	-

Results And Discussion

Energy and level width of $^{5}_{2}He$ system

Our purpose is to investigate the energy and level width of $^{5}_{2}He$ system by using the complex scaling method. The complex-scaled Hamiltonian matrix elements are diagonalized and we obtained the complex energy eigenvalues. The number of the basis state is determined to converge the solutions.

In complex scaling method, the continuum states vary with the 2θ dependence. This distribution of continuum eigenvalues depends on the choice of the number of basis. The resonance states for ($J^{\pi}=3/2^{-}$) can be seen clearly from the continuum states θ=20° to 40°. The calculated resonance energy of $^{5}_{2}He$ ($J^{\pi}=3/2^{-}$) system is 0.747 MeV and level width is 0.596 MeV.

From our calculation, we found that bound state and resonance state are discrete and obtained independently of θ. Resonance energy for $^{5}_{2}He$ ($J^{\pi}=3/2^{-}$) system is compared with the experimental result (D.R.Tilley, 2002) of resonance energy 0.798±0.008 MeV and level width 0.648±0.006 MeV. Energy levels diagram for $^{5}_{2}He$ ($J^{\pi}=3/2^{-}$) state by comparing with the experimental value is shown in Fig. 2. Our calculated results for the energy and level width of $^{5}_{2}He$ ($J^{\pi}=3/2^{-}$) system is consistent with the experimental results.

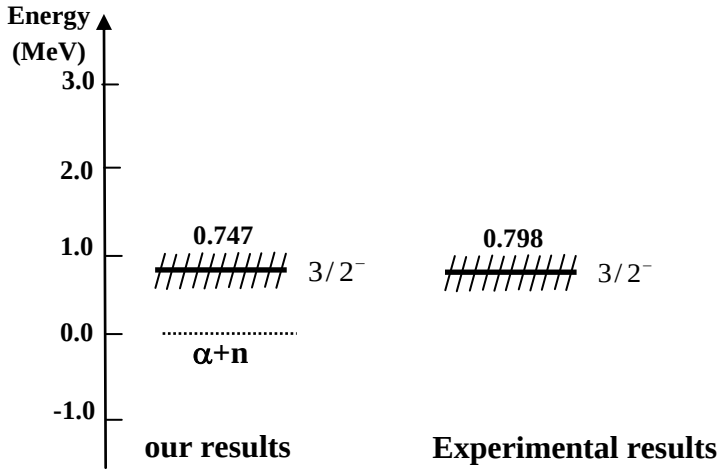

Fig. 2 Energy level of ^{5}He system in comparison with experimental value

Conclusion

The energy and level width of $^{5}_{2}He$ are calculated by using the complex Scaling method. From our calculation, we found that the position of resonance states in the complex energy plane remains almost unchanged with the variation of rotation angle θ. Our calculated results for the energy and level width of $^{5}_{2}He$ system are consistent with the experimental results.

Acknowledgement

The authors would like to express their sincere thank to Professor Dr Khin Swe Myint , Rector (Rtd.), Emeritus Professor, Department of Physics, University of Mandalay for her valuable advice and helpful discussion in this research work. The authors would like to thank Dr Aung Kyaw Thin, Rector, Banmaw University, for his permission to perform this research. The authors would like to thank Professor Dr Than Than Lwin, Head of Physics Department, Banmaw University, for her encouragement.

References

Anderson, H.L. *et al*., (1952). Phys. Rev. **85,** 936.

Aguilar, J. and Combes, J.M. (1971). Commun Math. Phys. **22,** 269.

Bohr, A. (1951) . Phys. Rev. **81,** 134.

Gyarmati, B. and Kruppa, A.T. (1985) Phys. Rev. **C 34**, 1.

Gaffney, L.P. *et al.*, (2013).Nature **497**, 199.

Kanada, H. *et al*., (1979). Prog. Theor. Phys. **61,** 1327.

Kallunkathariyil, J. and Sosin, Z. (2013). Int. J. Phys. **6**.

Tilley, D.R. *et al.,* (2002). Nucl. Phys. **A 708,** 3.

Microcontroller Based Water Tap Control System

Maung Maung Soe[1], Yi Yi Swe[2]

Abstract

The microcontroller based water tap control system is designed and constructed using ultrasonic sensors, PIC microcontroller, DC motor, motor driver circuit, amplifiers circuits and other electronic components. A pair of ultrasonic sensors (transmitter and receiver) is the main part of the system to detect an existence of an object under the water tap. The ultrasonic sensors are mounted side by side over the water tap and pointed to the downward direction. The ultrasonic transmitter circuit sends the ultrasonic wave. The ultrasonic receiver circuit accepts that signal as an echo when an object enters a predefined place. The microcontroller sends control signals to the motor drive circuit when it receives object detect signals from the ultrasonic receiver circuit. The DC motor is applied to turn the water tap. The range of ultrasonic detection is set to detect an object up to about 30 cm from the sensors. The constructed system can be used to open automatically the water tap of the basin when the hand or any other objects is put under the tap.

Key words: water tap, ultrasonic sensors, PIC microcontroller, transmitter, receiver, echo

Introduction

Industrial process control is a fascinating and challenging area of electronics technology and nothing has revolutionized this area like the microcontroller. The microcontroller has added a level of intelligence to the evaluation of data and a level of sophistication in the response to process disturbances. Microcontrollers are embedded as the "brains" in both manufacturing equipment and consumer electronic devices.

Process control relies on gathering input information, evaluating it, and initiating action. In industrial control, input information most often involves monitoring field devices whose outputs are one of two possible states.

The outputs of a microcontroller can be used to control the status of output field devices. Output devices are those devices that do the work in a process-control application. They deliver the energy to the process under control. A few common examples include motors, heaters, solenoids, valves, and lamps.

Continuous process control involves maintaining desired process conditions. Heating or cooling objects to a certain temperature, holding a constant pressure in a steam pipe, or setting a flow rate of material into a vat in order maintain a constant liquid level, are examples of continuous process control.

In this research work, the microcontroller based water tap control system is presented. The block diagram of the microcontroller based water tap control system is shown in Figure 1. Basically, the system consists of two separate sections: ultrasonic transmitter and ultrasonic receiver sections.

1 Dr, Associate Professor, Department of Physics, Banmaw University
2 Dr, Lecturer, Department of Physics, Yadanarbon University

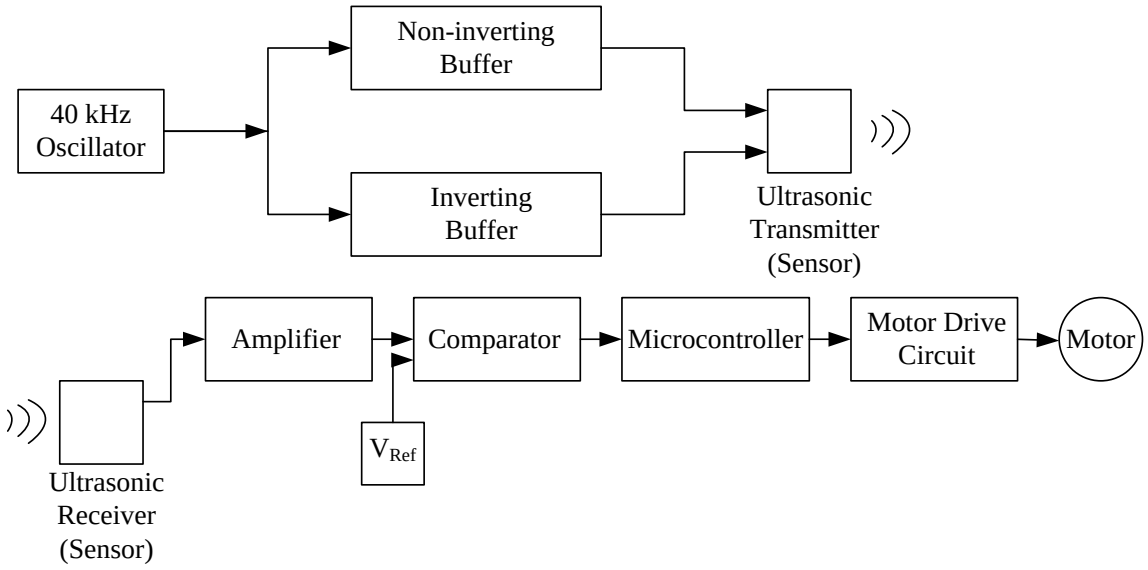

Figure 1 The block diagram of the microcontroller based water tap control system

The transmitter section is responsible to transmit ultrasonic wave of about 40 kHz signal through the open air. It consists of ultrasonic sensor (transmitter), oscillator and amplifier circuits. The main task of the receiver section is to accept the signal from the transmitter circuit and to process the signal with the help of the microcontroller circuit. The microcontroller circuit will produce appropriate drive signal to the motor driver circuit. The receiver section consists of the ultrasonic sensor (receiver), amplifier, comparator, microcontroller, motor driver circuit and dc motor.

A water tap, comprising a casing having a water intake pipe at one end connected to a water supply, a water outlet hole at an opposite end. The proposed system used two ultrasonic emitter and detector pairs to determine the existence of an object. This combination detects the object by emitting an ultrasonic wave that would reflect off an object and return to the detector.

An ultrasonic sensor is used for proximity detection of the reach of hands. A motor drive circuit is used to drive the motor which is attached to the water tap. A control circuit board controlled by microcontroller is used to drive a motor control water supply mechanism to close or open the center hole of water control valve. The motor-control water supply mechanism comprises a motor having a bolt coupling connected to the shaft of the water tap. The ultrasonic sensor detects the presence of user's hands to trigger control circuit board to drive motor to rotate clockwise for a measured time so as to drive water stop control rod to carry stub rod to leave away from the center hole of control valve permitting flow of water to pass through water outlet hole. The control circuit board triggers motor to rotate counter-clockwise for a measured time when user's hands leave away, so as to drive water stop control rod to move stub rod to insert in the center hole of control valve to further block up water passage.

Design and Construction

The design and construction of the microcontroller based water tap control system is explained in this section. The constructed system can be divided into two main parts: electronic circuits and control mechanism. The electronic circuits can be further divided into two sub sections: ultrasonic signal transmitter circuit and ultrasonic signal receiver and controller circuit.

The ultrasonic signal transmitter circuit

The ultrasonic signal transmitter circuit consists of 40 kHz oscillator circuit, inverting and non-inverting buffer circuits and ultrasonic transmitter. The circuit is shown in Figure 2. Two NOR gates (N1 and N2) and resistors (R1 and R2), capacitor (C1) and preset resistor (PR1) form the oscillator circuit. The values of capacitor and preset resistor determine the oscillation frequency of the oscillator circuit. The preset resistor is adjusted so that to obtain the oscillation frequency of about 40 kHz, which is required for ultrasonic sensor. The oscillator output is fed to the inverter gates (N3, N4 and N5 combination) in two different paths as shown in figure.

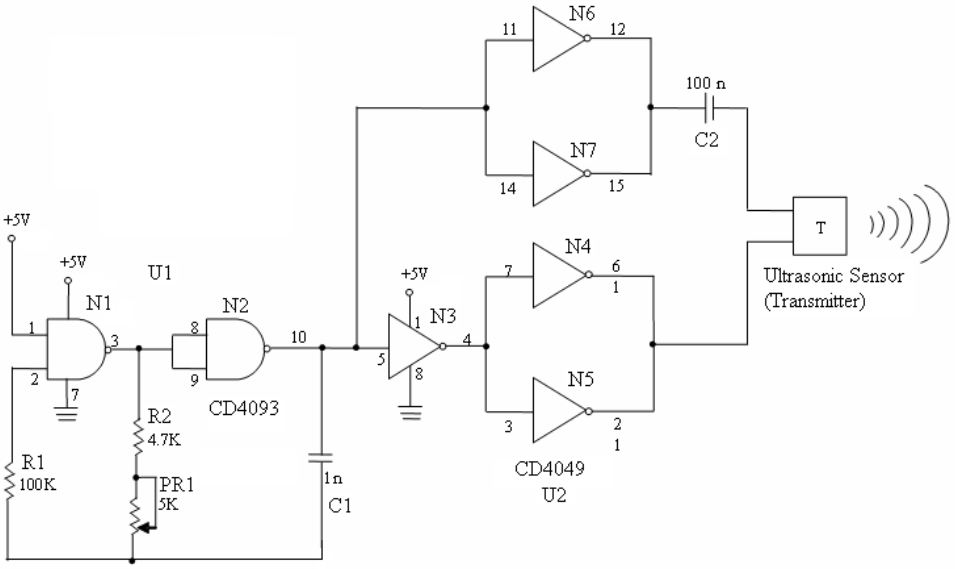

Figure 2 The ultrasonic transmitter circuit

The gates N4 and N5 are connected in parallel to obtain more power from the gate outputs. Similarly, the gates N6 and N7 are connected in parallel. The signal outputs at gates N4, N5 combination and gate N6, N7 combination are in opposite due to gate N3. This results the doubling of the signals at the output. The gate outputs are then fed to the ultrasonic transmitter (sensor) via a small capacitor, C2 to block any dc component reaching to the sensor. This type of sensor is usually used with the AC signals. The dc components directly fed to the sensor can permanently destroy the sensor. The sensor, then, converts the electrical signal into the acoustic wave and transmits through the air.

The ultrasonic signal receiver and controller circuit

The ultrasonic signal receiver and controller circuit is shown in Figure 3. It mainly consists of ultrasonic receiver (sensor), amplifier, comparator, microcontroller, motor drive circuit and dc motor. The ultrasonic receiver (sensor) accepts the ultrasonic wave (acoustic wave) coming into the receiving cone of the sensor. The sensor, then, converts the acoustic wave into corresponding electrical signals.

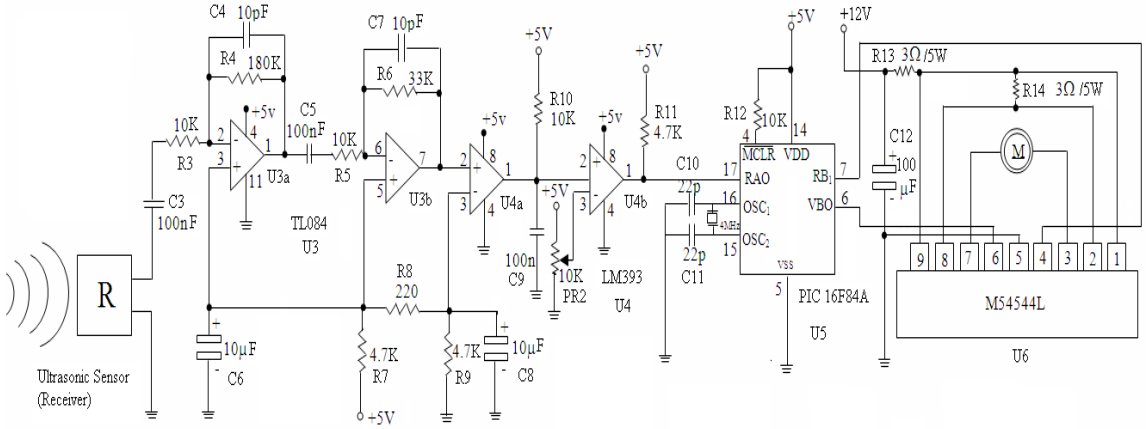

Figure 3 The ultrasonic signal receiver and controller circuit

The electrical signal at the output of the sensor is too weak to be applicable to the other circuits directly. Therefore the amplifier circuit must be installed immediately after the sensor circuit to obtain enough signal strength. The amplifier circuit is constructed by using TL084 operational amplifier IC (U3).There are two stages in the amplifier circuit. The first stage of the amplifier is designed as inverting amplifier with a gain of about 18. The voltage reference at non-inverting terminal is set to about 2.5 V by using the resistor voltage divider (R7, R8 and R9) instead of using ground reference. The output signal of amplifier U3 (a) is fed to the input of another inverting amplifier, U3 (b) with a gain of about 3.3. Therefore the overall voltage gain of the amplifiers is about 60.

The amplified signal is put to the non-inverting terminal of the comparator, U4 (a). The inverting terminal of the comparator is tied with the 2.5 V voltage reference. The square wave signal of equal duty cycle is produced from the comparator output when the amplified signal is present at the non-inverting terminal. The comparator output voltage swing between the 0 V and 5 V. The output of the comparator is fed the capacitor C9 to charge when the signal is present. The capacitor maintains the constant voltage of about 2.5 V when the signal input is present. On the other hand, the voltage across the capacitor is just 0 V when there is no signal input. The comparator U4 (a) output is also connected the non-inverting input of another comparator U4 (b). The voltage reference of the comparator is fed to the inverting input of the amplifier using preset resistor PR2. The preset resistor is adjusted so that to get the voltage reference of about 1.5 V. Therefore the comparator output is at logic "1" state (5 V) when the input signal at the ultrasonic sensor is present. The comparator output is at logic "0" state (0 V) when there is no input signal at the ultrasonic sensor.

The comparator U4 (b) output is fed to the RA0 pin of port A of the PIC 16F84A microcontroller (U5). The PIC microcontroller operates with 4 MHz crystal. The port A of the microcontroller is configured as input and port B is configured as output pins. The port B pins RB0 and RB1 are used to produce drive signals to the motor drive circuit. The microcontroller is programmed to produce appropriate drive signals to the motor drive circuit when the input signal is received at RA0 pin.

The motor drive circuit is constructed by using the driver IC U6. Two input pins of the motor drive IC are connected to the RB0 and RB1 pins of the microcontroller as shown in Fig. 3. The output pins of the motor drive IC is connected to the small dc motor (6 V motor). The motor will rotate in one direction (e.g. clockwise direction) if the RB0 is logic "1" and RB1 is logic "0". The motor will rotate another direction (e.g. counter clockwise direction) if the RB0 is logic "0" and RB1 is logic "0". The motor is in stop or no operation state if both inputs of motor drive circuit are in logic "0" state. The motor is in braking condition if both inputs are logic "1" state.

Control mechanism of the system

The dc motor is directly mounted on the water tap. The shaft of the motor is connected to the shaft of the water tap. The tap rotates to the counter clockwise direction (i.e. water tap is turn ON) when the dc motor rotates clockwise direction. The water tap rotates to the clockwise direction (i.e. water tap is turn OFF) when the dc motor rotates in counter clockwise direction. The motor is chosen so that it can turn ON and OFF the water tap without any difficulties. The water inlet pipe and water bar of the water tap are installed at the bottom part of the electronic circuits to avoid accidental short circuits due to possible water leakage from the water tape and pipes.

The Flow chart of the system

The flow chart of the system is shown in Figure 4. Firstly, the microcontroller's I/O ports are configured. The Port A pin (RA0) is set as input pin. It is used to accept the digital logic input from the ultrasonic receiver circuit. The RA0 pin is at logic "1" state if the object is detected by the sensor circuit. The RA0 pin is at logic "0" state if the object is not detected by the sensor circuit. The Port B pins (RB0 and RB1) are configured as output pins to produce dc motor drive signals for the motor driver circuit. The program set the Port B as decimal value "1" to drive the motor to the water tap close condition to ensure not to open the tap at the start. Then the motor is stopped after one second.

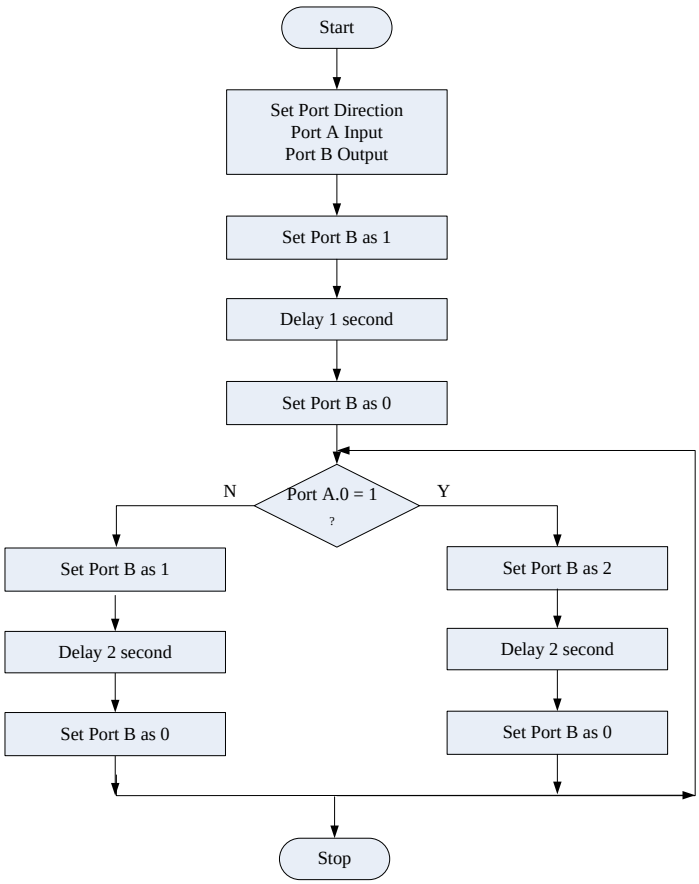

Figure 4 The flow chart of the system

The program, then, check the RA0 pin whether there is an object or not in front of the sensors. If RA0 is at logic "1", there is an object in front of the sensors and water tap is open by making Port B pins, RB1 = 1 and RB0 = 0. In this condition, the motor rotates in clock wise direction. If RA0 is at logic "0", there is no object and water tap is close by making Port B pins, RB1 = 0 and RB0 = 1. In this condition, the motor rotates in counter clock wise direction. The motor is stopped if both RB0 and RB1 pins are at logic "0" and "1" at the same time. The program will be repeated as long as the power is switch ON.

Results and Discussion

The automatic water tap control system, usually together with the automatic hand dryer, is widely used in hotels, super markets, office buildings, international air ports and housings. The microcontroller based water tap control system is designed and constructed. The internal circuitry of the system is shown in Figure 5. The bottom view of the water tap and ultrasonic sensors are shown in Figure 6. As can be seen in Fig. 5, the electronic circuits are well isolated from the water inlet and outlet sections. This prevents short circuit due to water leakage.

The arrangement of ultrasonic sensors can be seen in Figure 6. The sensors are mounted on the bottom part of the box making a small angle inward (about 30º). This arrangement of sensors ensures to detect an object (hand or cup) up to 30 cm distance. This is the reasonable distance for

the application of water tap. The transmitter produces ultrasonic wave and the receiver receives that signal if the hand (or any object) is entered in the detection region.

The distance of detection for an object can be increased if the sensors are mounted on the box with larger angles. The gain of the amplifier circuit of the ultrasonic receiver circuit is also set to about 60 to be consistent with the object detection distance. If the gain of the amplifier is increased, the distance of objection can be increased. The water tap is chosen so that the small dc motor can turn ON and OFF quite easily.

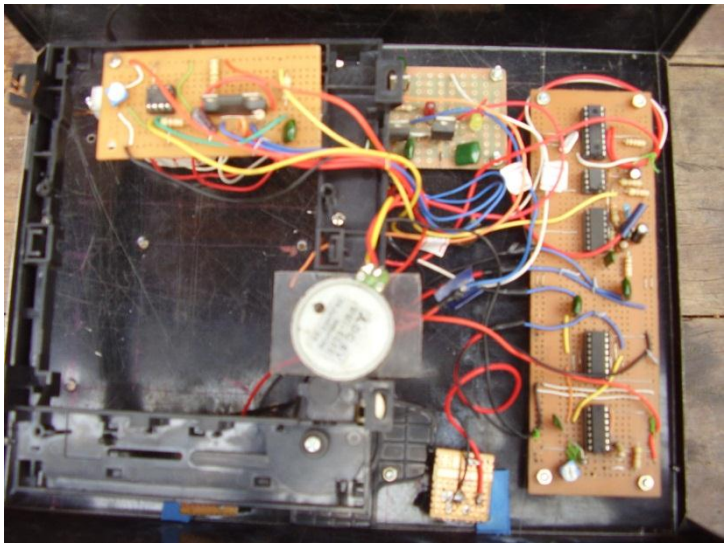

Figure 5 The internal circuitry of the water tap control system

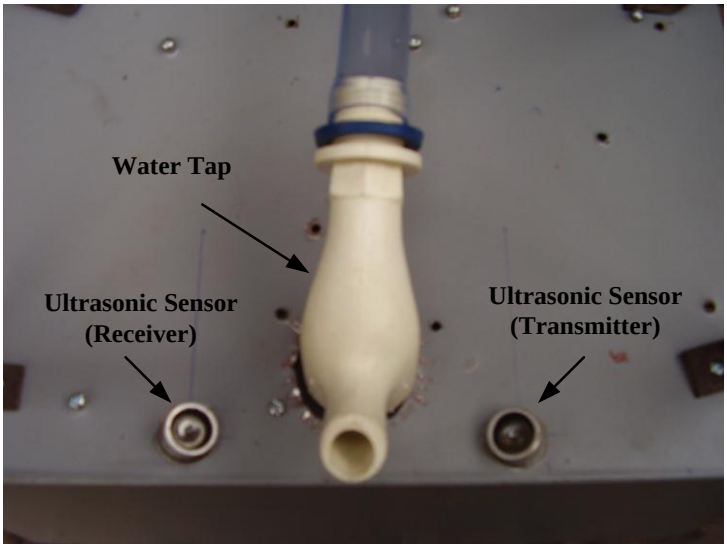

Figure 6 The bottom view of the water tap control system showing the water tap and sensor arrangements

Conclusion

The constructed water tap control system is intended for only demonstration purpose. It can turn ON and OFF water tap automatically when an object is put under the tap. The performance of the constructed water tap control system can be upgraded to commercial system by changing drive mechanism, drive motor and sensor arrangements and so on. The system can also be modified for further applications such as automatic hand dryer, automatic watering system in the toilet room and bath room. Infra red sensors can be used instead of ultrasound sensors in some conditions to suit real world applications.

Acknowledgements

I would like to express my special thanks to Dr Aung Kyaw Thin, Rector and Dr Aye Aye Han, Pro Rector, Banmaw University for their kind permission to carry out this research work. I am grateful to Professor Dr Than Than Lwin, Head of Department and Professor Dr Thaung Yi, Department of Physics, Banmaw University for their helpful advice and continuous encouragement. I also wish to express my sincere appreciation to all teaching staff from the Department of Physics, Banmaw University and all the persons who have helped me with this research.

References

[1] D. Ibrahim (2006) “PIC BASIC Projects”, (Burlington: Elsevier)

[2] G. McComb (2001) “The Robot Builder’s Bonanza”, 2nd ed., (New York: McGraw-Hill)

[3] Philips Semiconductors (2002) “LM 393 Low Power Dual Voltage Comparator Data Sheet”

[4] J. Kassan and J. Morelli (2005) “Ultrasonic Sensing for Challenging Environments”, http://www.sensorsmag.com

[5] P. Horowitz and W. Hill (1995) “The Art of Electronics”, 2nd ed., (Cambridge University Press)

[6] T.L. Floyd (2007) “Electronic Devices”, 7th ed., (New Jersey: Prentice-Hall)

[7] Microchip Technology Inc. (2001) “PIC 16F84A Data Sheet”, http:// www.microchip.com

Design and Construction of Stroboscope Based on PIC Microcontroller

Maung Maung Soe[1], Yi Yi Swe[2]

Abstract

The stroboscope using the electronic strobe method for the measurement of frequency for a rotating object is designed and constructed. The constructed stroboscope mainly consists of PIC 16F887 microcontroller, 16 x 2 line liquid crystal display (LCD) module, high power super bright LED, 555 timer circuit and other electronic components. The frequency and PWM (pulse width modulation) of the circuits are controlled by using two variable resistors. The signal output is sent to the LED driver circuit as well as the microcontroller circuit. The super bright LED produces flashing light corresponding to the generated frequency and PWM. The microcontroller counts the frequency of the signal and displays the frequency in hertz (Hz) and revolution per minute (RPM) units on the LCD module. The flashing LED is pointed to the rotating object whose speed is to be measured. The frequency and PWM are adjusted until the still image of the rotating object is obtained. The stroboscope is designed to measure the RPM of the object from 240 to 1500 RPM. The constructed LED stroboscope can measure the speed of the rotating object from the distance of up to 2 m using non-contact method.

Key words: stroboscope, super bright LED, microcontroller, liquid crystal display (LCD)

Introduction

Stroboscope is a device for studying the motion of a body, especially a body in rapid revolution or vibration, by making the motion appears to slow down or stop, as by periodically illuminating the body or viewing it through widely spaced openings in a revolving disk. A stroboscope also known as a strobe is an instrument used to make a cyclically moving object appear to be slow-moving, or stationary. It consists of either a rotating disk with slots or holes or a lamp such as a flashtube which produces brief repetitive flashes of light. Usually the rate of the stroboscope is adjustable to different frequencies. When a rotating or vibrating object is observed with the stroboscope at its vibration frequency (or a submultiple of it), it appears stationary. Thus stroboscope is also used to measure frequency and RPM (revolution per minute). It is an instrument producing a flashing light, the frequency of which can be synchronized with some multiple of the frequency of rotation, vibration, or operation of an object, etc, making it appear stationary. It is also used to determine speeds of rotation or vibration, or to adjust objects or parts.

The stroboscope works by producing very brief yet very bright pulses of light. If the frequency of the light pulses is correct, the rotating object will be illuminated at the same position during each flash of light, giving the appearance that is stationary. This phenomenon is called the stroboscopic effect. The actual rotational speed will be downshifted to zero in the eyes of the observer, giving the false perception that the object is standing still. The object will also appear stationary when the strobe frequency is some integer fraction of the rotational frequency, such as one half, one third, or one forth, etc. This is because these cases will also result in the object being

1 Dr, Associate Professor, Department of Physics, Banmaw University
2 Dr, Lecturer, Department of Physics, Yadanarbon University

illuminated when it is in the same position each time. If the strobe frequency is slightly lower or higher than the rotational rate (or an integer fraction of the rotational rate) of the object, it will appear to rotate slowly forward or backward. In these cases the rotational speed has been downshifted to a speed slightly greater than zero in the eye of the observer. As the strobe frequency is swept, the observer may notice several points at which the rotation appears to first slow, then stop, and then begin rotating in the opposite direction.

The stroboscope mainly consists of variable frequency and pulse width modulator (PWM) circuits, microcontroller, LCD module, voltage regulator; LED driver circuit and high power super bright LED. The frequency and PWM of the circuit are controlled by using two variable resistors. The signal output is sent to the LED driver circuit as well as the microcontroller circuit. The super bright LED produces flashing light corresponding to the produced frequency and PWM. The microcontroller counts the frequency of the signal and displays the frequency in hertz (Hz) and revolution per minute (RPM) units on the LCD module. The flashing LED is pointed to the rotating object whose speed is to be measured and the frequency and PWM are adjusted until the still image of the rotating object is obtained. The regulated power supply supports necessary voltages to the other circuits. The functional block diagram of the constructed stroboscope is shown in Figure 1.

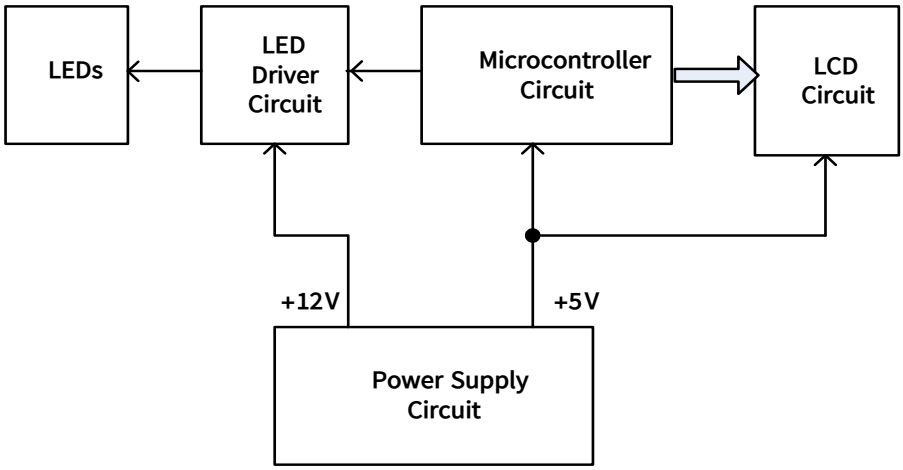

Figure 1 The functional block diagram of the constructed stroboscope

Electronic Devices Used in this Research Work

The constructed stroboscope mainly consists of the PIC 16F887 microcontroller, the 16 x 2 lines LCD module, LM 7805 voltage regulator, TIP122 transistor, 10 W super bright LED and 555 timer circuit. The general features and necessary theory background of the components used in the present research work will be presented in this section.

The PIC 16F887 microcontroller

Microcontrollers contain all the components required for a processor system in one chip: a CPU, memory and I/O. A complete system can therefore be built using one MCU chip and a few I/O devise such as a keypad, display and other interfacing circuits. Now, it will be seen how this is done in our typical microcontroller.

The PIC16F887 is a 40-pin device and is one of the popular microcontrollers used in complex applications. The device offers 8192 x 14 flash program memory, 368 bytes of RAM, 256 bytes of non-volatile EEPROM memory, 36 I/O pins, 14 analogue capture and comparator circuits, USTART, and external interrupt facilities. The pin configuration of the PIC16F887 is shown in Figure 2.

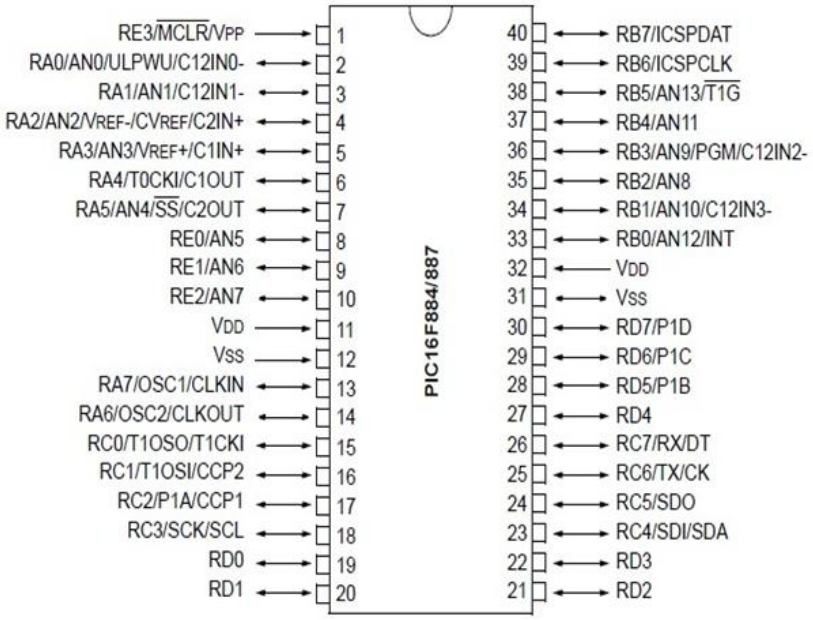

Figure 2 The pin configuration of the PIC16F887 microcontroller

The 16 x 2 lines LCD module

A liquid crystal display (LCD) is an electronic device that can be used to show numbers, texts and measurement data. There are two main types of LCD display, numeric displays and alphanumeric text displays.

The display is made up of a number of shaped 'crystals'. In numeric displays these crystals are shaped into 'bars', and in alphanumeric displays are shaped into 'dots'. Each crystal has an individual electrical connection so that each crystal can be controlled independently. When no current is passed through the crystal, it reflects the same amount of light as the background material, and so the crystals cannot be seen. When the crystal has an electric current passed through it, it changes shape and so absorbs more light. This makes the crystal appear darker to the human eye and so the shape of the dot or bar can be seen against the background.

The LCD display used in the circuit is GDM 1602A module. It can display 16 x 2 characters and it is possible to produce a readout using 8 x 80 pixels of the display. The LCD can displays a standard ASCII set of characters plus Japanese, Greek and mathematical symbols.

The 7805 voltage regulator

This series of fixed-voltage integrated-circuit voltage regulators is designed for a wide range of applications. These applications include on-card regulation for elimination of noise and distribution problems associated with single-point regulation. Each of these regulators can deliver up to 1 A of output current. The internal current-limiting and thermal-shutdown features of these regulators essentially make them immune to overload. In addition to its use as fixed-voltage regulators, these devices can be used with external components to obtain adjustable output voltages and currents, and also can be used as the power-pass element in precision regulators.

TIP122 transistor

The TIP122 transistor is a NPN Epitaxial Darlington Transistor. It also known as a Darlington pair, consists of a pair of bipolar transistors that are connected in order to provide a very high-current gain from a low-base current. In a Darlington transistor, the input transistor's emitter is wired to the output transistor's base and their collectors are tied together. Therefore, the current that is amplified by the input transistor is amplified even further by the output transistor. The TIP122 is also used in medium power linear switching applications.

The 555 timer

The 555 timer is astable multivibrator chip, which will operate at DC power supply potentials from +5V DC to +18V DC. The output of the 555 can either sink or source up to 200mA of current. The switching speed is $100ms^{-1}$. The 555 operate in two different modes, monostable (one short) and astable (free running). The inputs include threshold, trigger, control voltage, discharge and reset. Pin diagram of 555 timer is shown in Figure 3.

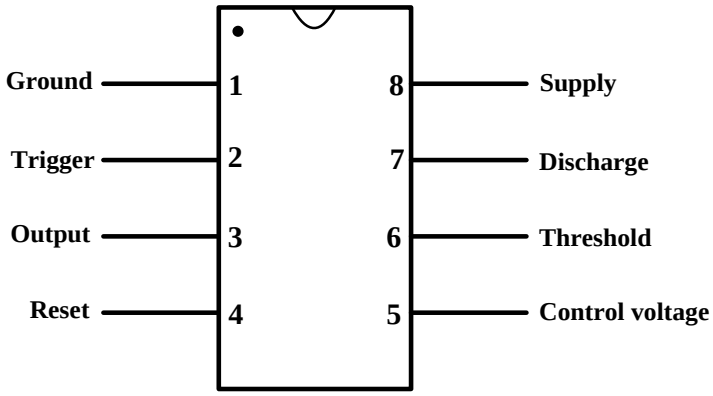

Figure 3 Pin diagram of 555 timer

Design and Construction of the Stroboscope

The constructed stroboscope mainly consists of the 555 timer circuit, the microcontroller circuit, the LCD display circuit, power supply circuit and the LED driver circuit. Operation of each circuit will be explained in this section. The complete circuit diagram of the constructed stroboscope is shown in Figure 4.

The 555 timer circuit mainly consists of two 555 timer ICs. One IC is connected as an oscillator (astable multivibrator circuit) and other IC is used as a PWM controller circuit. The preset resistor (100 KΩ) is used to control the frequency output of the oscillator circuit. The capacitors (2 μF and 1 μF) are connected with the pin 2 of the 555 timer IC to adjust the frequency output. The capacitors are connected with the timer using single pole double throw switch. The frequency output from the oscillator varies from 4 Hz to 14 Hz if the 2 μF capacitor is connected with the timer IC. The frequency output from the oscillator varies from 12 Hz to 25 Hz if the 1 μF capacitor is connected with the timer IC. The PWM controller circuit is used to control the ON time and OFF time of the frequency output from the oscillator circuit. The preset reset resistor (250 KΩ) and the capacitors (1 μF and 0.47 μF) are used to adjust the ON time of the frequency output.

The PIC 16F887 microcontroller is the main part of the circuit. It is operated with 10 MHz clock signals produced using crystal oscillator. The port B pin (RB0) of the microcontroller is configured as input pins. The RB0 pin is connected with the output pin of the 555 timer IC circuit. The RB0 pin receives frequency from the 555 timer circuit. The microcontroller counts the frequency of the RB0 pin. The port D pins are programmed as output pins. The Port D pin RD2 is connected with the RS pin of the LCD module. The Port D pin RD3 is connected with the E pin of the LCD module. The Port D pins (RD4-RD7) are connected with the data pins (D4-D7) of the LCD module. The measured frequency in hertz (Hz) and revolution per minute (RPM) values are sent to the LCD module.

The main task of the LCD display circuit is to display the measured frequency and RPM of the rotating object. The LCD module is configured to work in 4-bits mode to safe useful microcontroller pins. The upper line of the LCD module is programmed to display the measured frequency in hertz as "F = --- Hz" and the lower lines is programmed to display the revolution per minute (RPM) as "RPM = ---".

The LED driver circuit consists of the TIP 122 Darlington power transistor and 10 W super bright LED. The base terminal of the transistor is connected with the output of the 555 timer circuit. The emitter of the transistor is grounded. The collector of the transistor is connected with the cathode terminal of the LED. The anode terminal of the super bright LED is connected to the + 12 V power supply via 20 Ω (5 W) current limiting resistor. The voltage drop across the LED is about 8.8 V. The current passing through the LED is about 150 mA. The transistor acts as an electronic switch in this circuit. The collector-emitter junction can be considered as a switch. The base-emitter junction of the transistor is forward-biased and the transistor is turned ON if the oscillator output is at logic '1'. The switch is CLOSE and the collector is connected with the ground. Therefore the current from the + 12 V supply is flowed through the LED via current limiting resistor to the ground. The LED produces bright light in this condition. The base-emitter junction is reverse-biased and the transistor is turned OFF if the oscillator output is at logic '0'. The switch is OPEN and there is no current passing through the LED. Therefore the LED light is turned OFF.

The power supply circuit used in the complete circuit is the + 5 V regulated power supply. The main component of the circuit is 7805 regulator IC. It is the three terminal device having one input, one output and one ground terminal. The DC voltage obtained from the 12 V battery is fed to the input terminal of the 7805 IC. The + 5 V regulated voltage is obtained from the output terminal. Two small capacitors are used to filter out unwanted noises. The + 5 V is used to supply

the microcontroller, LCD module and the 555 timer circuit. The + 12 V supply is used for the LED driver circuit.

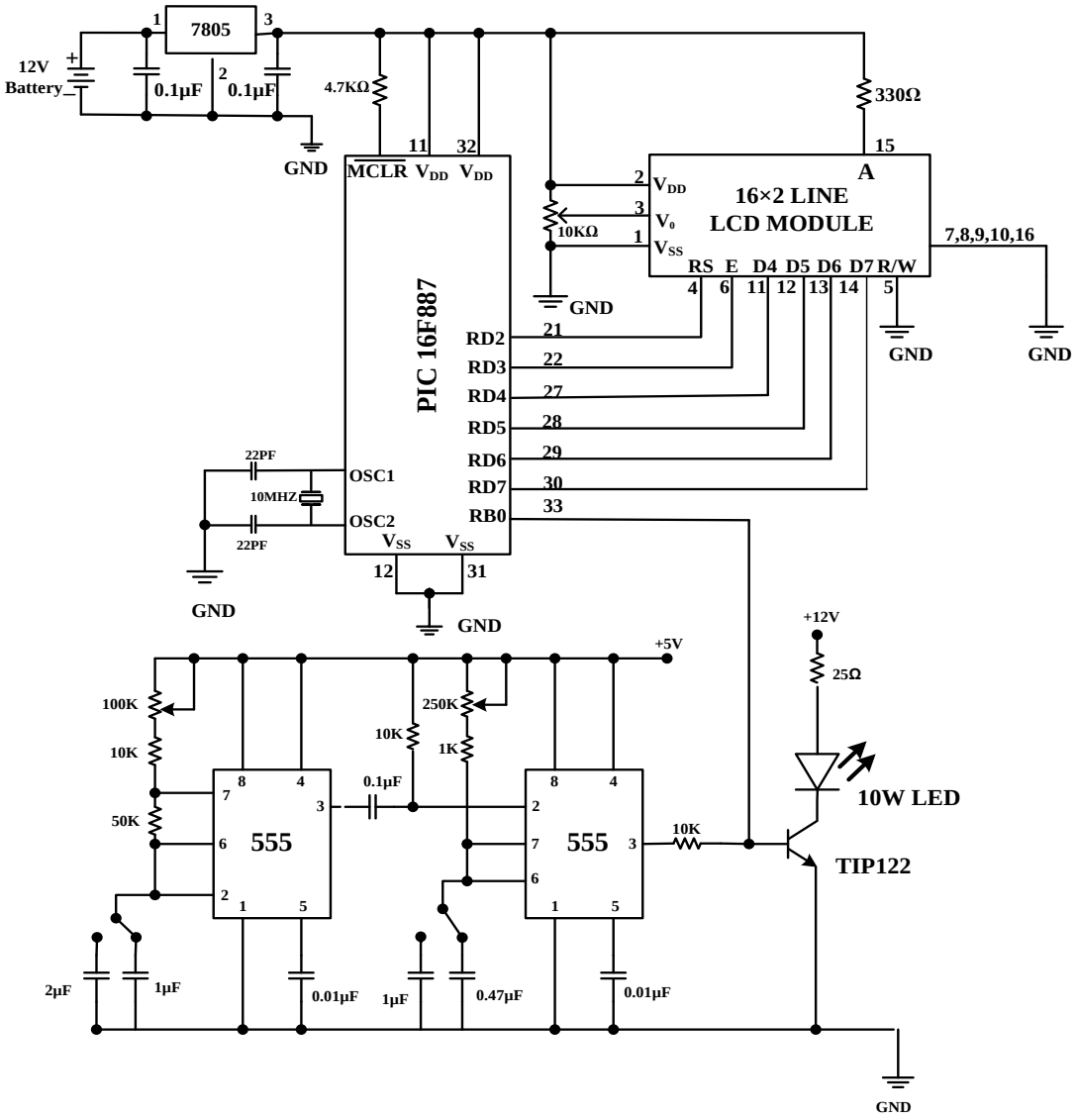

Figure 4 The complete circuit diagram of the stroboscope

The Flowchart of the Stroboscope

The flowchart of the stroboscope is shown in Figure 5. The program starts by setting the I/O ports, LCD pins and mode. Then the frequency and PWM output of the timer oscillator is adjusted. The frequency output is sent to the LED driver circuit to produce flashing light. The light source is pointed to the rotating object. If the still picture of the object is obtained, the frequency adjustment is stopped and then display measured frequency on the upper line of the LCD module in "Hz". The measured frequency is converted into RPM (revolution per minute) by multiplying it by 60. The RPM of the rotating object is also displayed on the lower line of the LCD module.

Then the program waits a few seconds before going back to the start of the frequency adjusting section. The program is repeated as long as the power is turned ON.

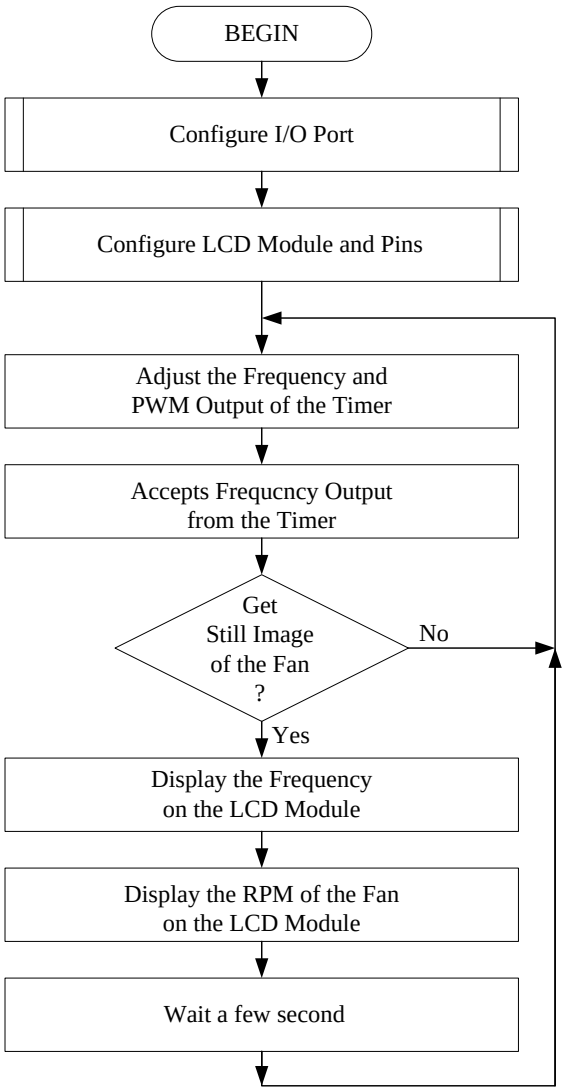

Figure 5 The flow chart diagram of the stroboscope

Results and Discussion

The constructed stroboscope is used to measure the frequency and rpm of the rotating or vibrating object. The LED light source used in this research work is 10 W 900 LM high bright LED light lamp chip which is constructed using 9 surface mounted LEDs in 3 x 3 arrays in a single package. The light source is then focused using small plano-convex lens. The rotating fan is accepted the flashing light from the stroboscope. Then the frequency and PWM output of the oscillator is adjusted until the still image of the rotating fan is obtained. The stroboscope measured the speed of the rotating fan by using non-contact method. The constructed stroboscope can measure the rotating speed from the distance up to 2 m away from the object. The stroboscope is

designed to measure the RPM of the object from 240 to 1500 RPM. Photographs of the different views of the constructed stroboscope are shown in Figure 6 (a) and Figure 6(b), respectively.

(a) Internal circuit diagram (b) upside view

Figure 6 The photograph of the constructed stroboscope

Conclusion

In this research work, the stroboscope for the measurement of frequency and RPM is designed and constructed. The constructed stroboscope demonstrates the possibility of using it to measure the speed of the rotating and vibrating object. It is constructed as battery powered portable unit. Therefore it can be used in the field service as well as in the Lab. The range of the stroboscope can be enhanced by using more powerful LED light sources together with better focusing lens. The RPM range can also be raised by replacing more stable and wider frequency range oscillator circuit.

Acknowledgements

I would like to express my special thanks to Dr Aung Kyaw Thin, Rector and Dr Aye Aye Han, Pro Rector, Banmaw University for their kind permission to carry out this research work. I am grateful to Professor Dr Than Than Lwin, Head of Department and Professor Dr Thaung Yi, Department of Physics, Banmaw University for their helpful advice and continuous encouragement. I also wish to express my sincere appreciation to all teaching staff from the Department of Physics, Banmaw University and all the persons who have helped me with this research.

References

[1] D. Ibrahim (2006) “PIC BASIC Projects”, (Burlington : Elsevier)

[2] T.L. Floyd (2007) “Electronic Devices”, 7th ed., (New Jersey : Prentice-Hall)

[3] Microchip Technology Inc., “PIC 16F887 Data Sheet”, (2001). http://www.microchip.com

[4] XIAMEN OCULAR, “GDM 1602A Liquid Crystal Display (LCD) Data Sheet”, (2010). http://www.xmocular.com/MODULE/GDC1602A.htm

Automation Using Bluetooth, Android And Arduino

Zin Zin Naing[1], Khin Htwe[2], Lai Lai Win Hlaing[3]

Abstract

The electrical appliances can be controlled by android smart phone from the remote location (within 30ft in diameter). Bluetooth, android smart phone and Arduino microcontroller are used in this home automation system. Bluetooth device HC-05 is connected to the Arduino. And then, it is paired to the android phone via Bluetooth technology. Bluetooth HC-05 receives the message sent from android phone and sends to Arduino microcontroller. As soon as the main processing unit, Arduino, receives the information from Bluetooth, it makes the processing to control the home appliances "ON "or "OFF". EEPROM is used to store the relay's final status when the power is in failure so that system is operated in last memory status when the power has come up.

Keywords: Android, Arduino, Bluetooth, EEPROM and Processing unit.

Introduction

Nowadays, most of people have smart phones with them almost all the time. It makes opportunity to use these smart phones to control home appliances. This automation system uses Android application which is used to control electrical appliances with one touch. Commands are sent via Bluetooth to Arduino Uno. This application controls the various appliances connected to relays. When the toggle buttons on the application are pressed, corresponding signals are sent from your Android phone to the Bluetooth module which is connected to Arduino. The Arduino finds out which signal was sent and compares it to the predefined signals assigned for each appliance. When it identifies that signal, the Arduino activates hooked up to its digital pin by passing 5V through it. Thus the relay is switched corresponding appliance connected to the relay is turned ON as well. To switch passes a 0V or logic low to its digital pin.

Materials and Method

The home automation circuit consists of an Arduino Uno, Bluetooth module HC-05 and relays. The number of relays depends on the number of appliances to be controlled. Arduino Uno is powered with 12V or 9V DC adaptor. The relay module and Bluetooth module can be powered by using the built- in power supply of Arduino Uno.

Bluetooth Module

The Bluetooth used in this research is HC-05, which supports master and slave mode serial communication in USB or UART interface with baud rate lies between 9600 and 115200 as shown in Figure.1. Using these features it can communicate with other Bluetooth – enabled devices like mobile phone, tablet and laptop. Bluetooth wireless technology is becoming a popular standard in communication. It is one of the fastest growing fields in wireless technologies. It is convenient to use and has the bandwidth to meet most of today's demands for mobile and personal

1 Dr, Associate Professor, Department of Physics, Banmaw University
2 Dr, Associate Professor, Department of Physics, Banmaw University
3 Dr, Lecturer, Department of Physics, Banmaw University

communications (using short-wavelength UHF radio waves in the ISM band from 2.4 to 2.485GHz). Bluetooth technology handles the wireless part of the communication channel; it transmits and receives data wirelessly between these devices.

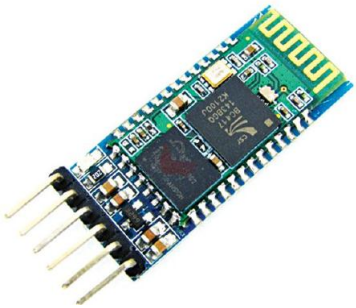

Figure.1 Bluetooth HC-05

It delivers the received data and receives the data to be transmitted to and from a host system through a host controller interface (HCI). The most popular host controller interface today is either a UART or a USB.

The Bluetooth module has 4 – pins: VCC, TX, RX and GND. VCC and GND are connected to 5V and ground from Arduino UNO. The Bluetooth module works on 3.3V but 5V power supply can provide to it because it has an on board 5V to 3.3V regulator. The TX and RX pins of the Bluetooth module must be connected to RX and TX pins of the Arduino. In Arduino UNO, any digital pins can be configured as RX and TX using software. Hence, TX of Bluetooth is connected to pin 4 of Arduino. But when connecting RX of Bluetooth to TX of Arduino (or any microcontroller as a matter of fact), we need to be careful as the pin can tolerate only 3.3V. But the voltage from TX or Arduino will be 5V.

The module has two modes of operation, Command Mode where one can send AT commands to it and Data Mode where it transmits and receives data to another Bluetooth module. The default mode is the DATA Mode, and this is the default configuration, which may work fine for many applications.

Relay Module

A relay allows turning on or turning off a circuit using voltage and/or current much higher than what Arduino could handle. Relay provides complete isolation between the low-voltage circuit on Arduino side and the high-voltage side controlling the load. It gets activated using 5V from Arduino, which, in turn, controls electrical appliances like fans, lights and air-conditioners.An 4-channel relay module is shown in Figure.2.

Baud Rate: 9600 bps, Data: 8 bits, Stop Bits: 1 bit, Parity: None, Handshake: None Passkey: 1234

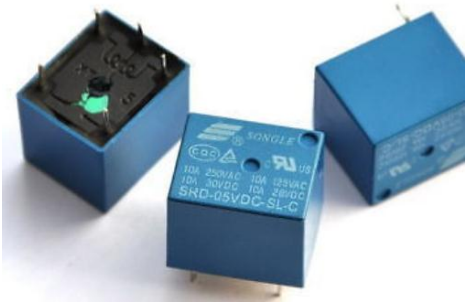

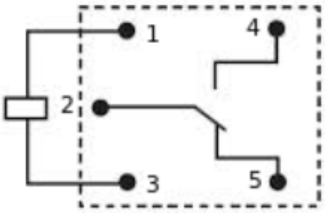

Figure.2 Relay and its pin layout

The relay using in this research is SPDT (single pole double throw), it has 5 pins on the underside. Pin 1 and pin 3 are the coil pins. Pin 2 is the common contact in the relay to which have to connect the power (AC 230V), and 4 is the pin to which have to connect appliance wire.

EEPROM

EEPROM is the acronym for Electronically Erasable Programmable Read Only Memory, which is used here to store the status of the relay (ON/OFF), so that in case of a power failure when the controller resets, all the relays which were kept ON will come back to their ON position after the power has come up. So whenever a relay is turned on, a variable stored in an address in the EEPROM changes it's value to 1 and whenever it's turned OFF the same variable changes to 0. Each relay has it's own variable assigned to store it's status in the EEPROM. So at the beginning of the code the first thing was to initialize the relays according to the values stored in the EEPROM.

Arduino Uno board

Arduino is an open source electronics prototyping platform based on flexible, easy-to-use hardware and software. It is intended for artists, designers, hobbyists and anyone interested in creating interactive objects or environments. Arduino Uno is based on ATmega328 microcontroller (MCU). It consists of 14 digital input/output pins, six analogue inputs, a USB connection for programming the onboard MCU, a power jack, an ICSP header and a reset button. It is operated with a 16MHz crystal oscillator and contains everything needed to support the MCU. It is very easy to use as you simply need to connect it to a computer using a USB cable, or power it with an AC-to-DC adaptor or battery to get started. The MCU onboard is programmed in Arduino programming language using Arduino IDE.

Operation

In this home automation circuit, Pins 10 and 11 of Arduino are connected to pins TXD and RXD of the Bluetooth module, respectively, as shown in Figure.3. Pins Gnd and V_{CC} of the Bluetooth module are connected to Gnd and +5V of Arduino board respectively. Pins 2, 4, 6 and 8 are connected to the four relays (RL_1, RL_2, RL_3 and RL_4) of the relay board. Pins Vin and Gnd of the relay board are connected to pins V_{in} and Gnd of Arduino board, respectively.

When the power is turned on, the connection LED on the Bluetooth module starts blinking. It needs to start the “Wiz Bluetooth Controller” application in smart phone and get connected to the Bluetooth module. If the pairing is successful, the LED becomes stable. Arduino-Android

connection in Figure 4. Photograph of experimental setup of Bluetooth controlled appliances is shown in the Figure 5.

Results and Discussion

This research is tested by help of Arduino (as shown in Figure.6 to 9) and all preliminary implementations are completed successfully. V_{in} is usually used to give input power, but since 5V is supplying to Arduino using an adaptor, V_{in} pin on Arduino can be used to power the 12V relay module. In this research, the output of relays is connected to LED which is provided by DC power supply just as a prototype model. These relay outputs can be connected to the home appliances which are connected to the ac main line. If the appliance with high power can be controlled by 12V relay addition to opto – coupler module for safe.

Conclusion

Bluetooth module is powered with 3.3 volts. Remember, the bare HC-05 run on 3.3V and not on 5V. On the other hand, the JY-MCU has a built in regulator, it can run on a 5V line. Wiz bluetooth app can be used only in Android phone and not for iphone with iOS software. And then, this app is only used in English language. The operation cannot implement properly in the strong electromagnetic field. The bluetooth HC-05 has 2mW and communicates in the range of 10 metres.

If the transmitter and receiver of bluetooth are connected to the default transmitter and receiver pin of D_1 and D_0 instead of D_{11} and D_{10} of Arduino, data collision can occur. When sketch is uploaded to Arduino, these pins are removed from Arduino because the data is uploaded through these pins. If not, sketch cannot be uploaded to Arduino.

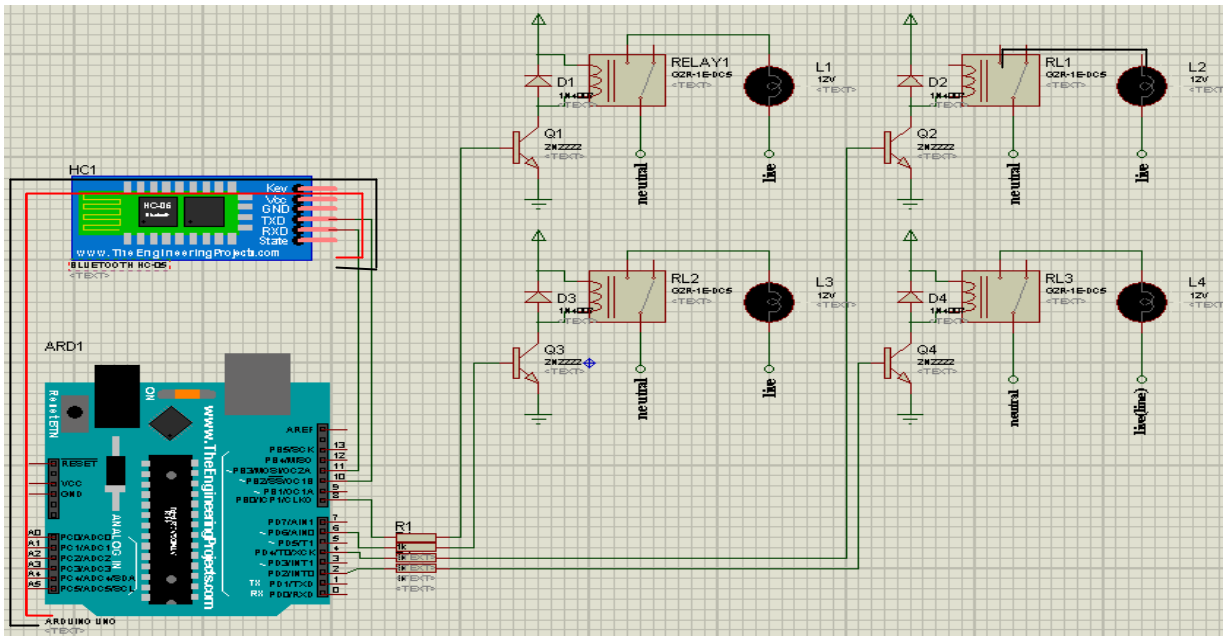

Figure.3 Schematic circuit diagram of home automation

Figure.4 Arduino – android connection

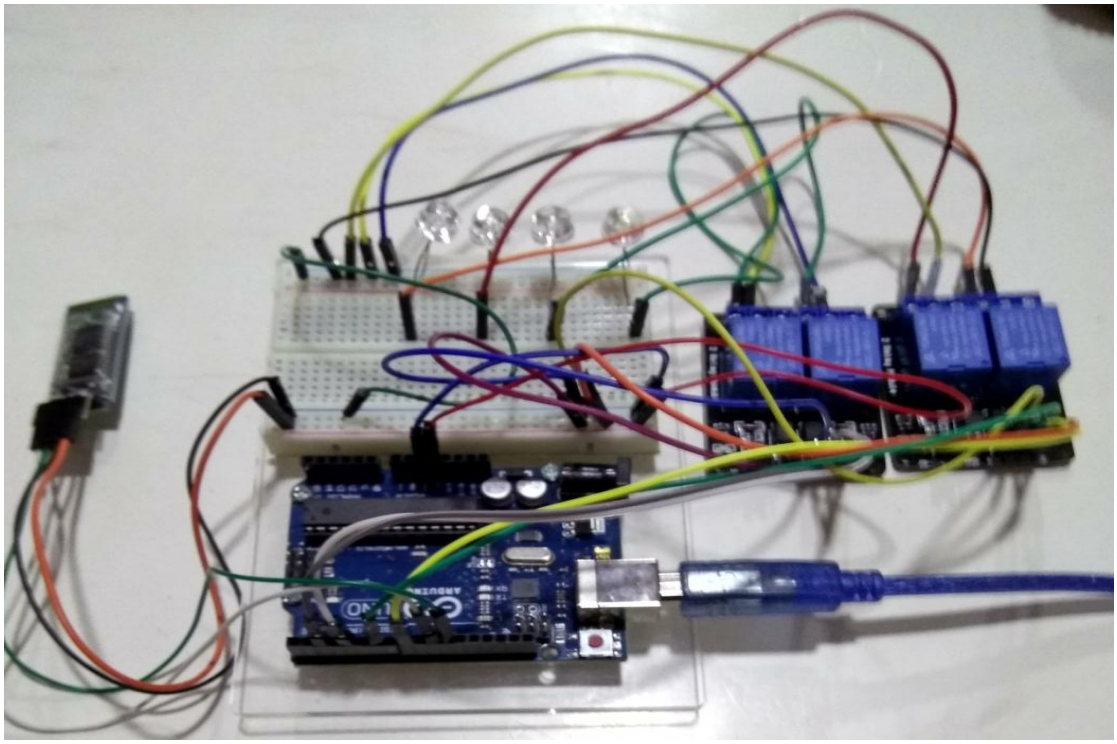

Figure.5 Experimental setup of Bluetooth controlled appliances

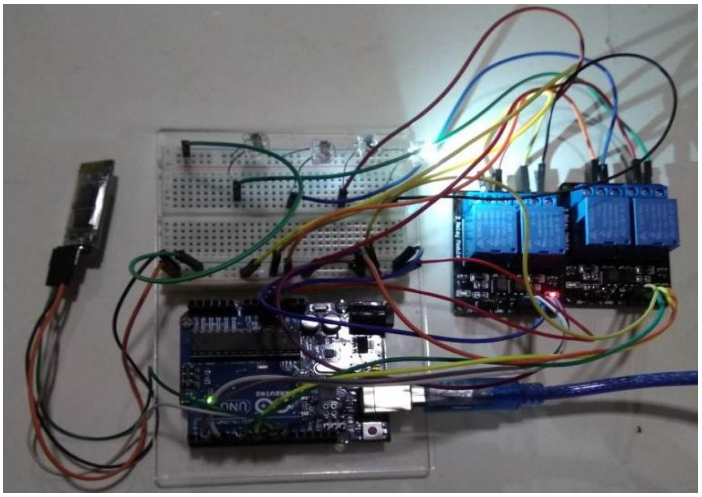

Figure.6 Relay 1 on

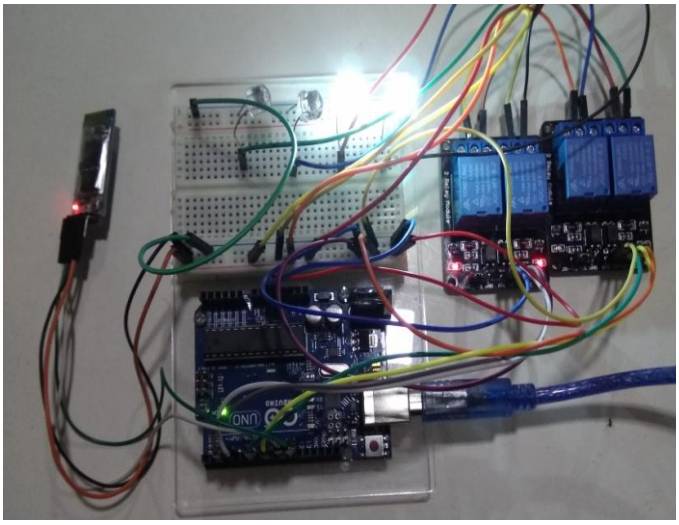

Figure.7 Relay 1 and 2 on

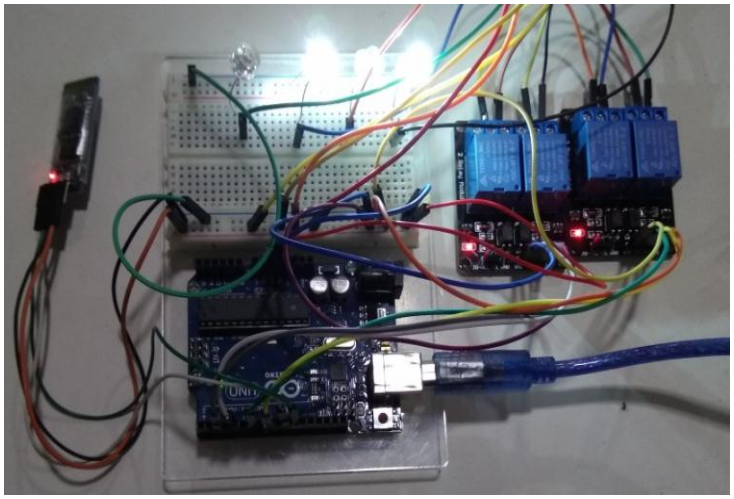

Figure.8 Relay1,2 and 3 on

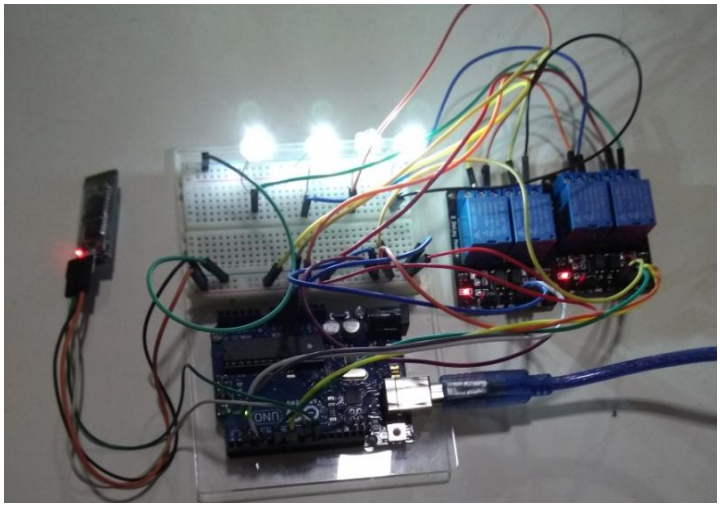

Figure.9 All relays are on

Acknowledgements

I wish to express my sincere thanks to Dr Aung Kyaw Thin, Rector and Dr Aye Aye Han, Pro-Rector, Banmaw University for their permission to do this paper. I am very grateful to Professor Dr Than Than Lwin, Head of Department of Physics, Banmaw University for her kind permission to carry out this research.

References

Banzi M, 2009"Getting Started with Arduino" U.S.A.

Boxall J, 2013 " Arduino Workshop", No Starch Press, San Francisco.

A , 2013 "Android™ Open Accessory Programming with Arduino" , John Wiley & son inc.

Monk S, 2010"Arduino™ + Android™ Projects for the Evil Genius" Tab.

Monk S, 2010 "30 arduino projects for the evil geneius" Mc Graw-Hill Companies, Inc.

Real Time Physical Data Logger

Zin Zin Naing[1], Khin Htwe[2], Lai Lai Win Hlaing[3]

Abstract

The data of temperature which is the output of LM 35 sensor are detected by the Arduino. At the same time, the current time can be interpreted by real time clock (RTC 1307 IC). Temperature with real time clock can be expressed on the serial monitor and can be stored in the SD card. Arduino Uno, data logger breakout, real time clock and LM 35 temperature sensor are used in logging the temperature with real time.

Keywords: RTC, logger, SD card and LM35.

Introduction

In this research, the physical data such as temperature with real time is displayed on serial monitor and stored in the micro SD card. Temperature which is produced by LM 35 is detected using Arduino microcontroller. Time is expressed by using RTC1307. The temperature with real time is logged in micro SD card. Microcontroller processes all functions of temperature detection, time expression and data logging.

LM 35 is the temperature sensor which produces an analog voltage directly proportional to the temperature with an output of 10mV per degree. The sketch converts the analog reading output into the millivolts and divides this to get degree Celsius. It can be also converted into degree Fahrenheit. The sensor accuracy is 0.5 °C and in many case it can be used in integer math instead of floating point.

SD card logger break out consists of the SD card which is used to store long term data. While the Arduino chip has a permanent EEPROM storage, its only a couple hundred bytes - tiny compared to a 2 GB SD card. SD cards are so cheap and easy to get, it is an obvious choice for long term storage.

The RTC (real time clock) is an I2C device, which means it uses 2 wires to communicate. These two wires are used to set the time and retrieve it. On the Arduino, the pins are 'fixed' to be Analog 4 and 5 for the built in I2C capability. The Arduino does have a built-in timekeeper called **millis ()** and there is also timers built into the chip that can keep track of longer time periods like minutes or days. A separate RTC chip is required because the **millis ()** only keeps track of time since the Arduino was last powered - that means that when the power is turned on, the millisecond timer is set back to “0”.

1 Dr, Associate Professor, Department of Physics, Banmaw University
2 Dr, Associate Professor, Department of Physics, Banmaw University
3 Dr, Lecturer, Department of Physics, Banmaw University

Materials and Method

Arduino Uno R3 board, LM 35 temperature sensor, SD card break out as data logger, real time clock, micro SD memory card, and USB printer cable, are main parts in the temperature logger with real time clock. SD, RTC, SPI and wire libraries are required to operate the data logger with RTC. The hardware will be a personal computer that can run the Arduino IDE (integrated development environment) software.

SD card logger

Setting it up is as simple as plugging the header pins from the microSD card adapter into Arduino. The microSD card adapter (as shown in Figure.1) is connected to the Arduino board. Digital pin 4, 11, 12 and 13 are connected to the CS, MOSI, MISO and CLK of microSD card adapter.

Figure.1 The front and back view of the microSD card adapter

At this research, the microSD card adapter use digital pins 4, 11, 12and 13, so one can't use those for anything else. For reference, all of the SD functions are handled by the SD library.

The microSD memory card

By using microSD cards with Arduino, one can capture data from many sources, such as the LM35DZ temperature sensor used. The microSD card can be also used to store web server data or any files. To record and store the data collected, a microSD memory card shield like the one can be used shown in Figure.2. This shield uses microSD (not microSDHC) cards with a capacity of up to 2GB.

Figure.2 A microSD card with a 2GB capacity

Real time clock (RTC)

A real time clock is basically just like a watch- it runs on a battery and keeps time even when there is a power outage. Using an RTC, it can keep track of long timelines, even if

microcontroller is reprogrammed or is disconnected from USB or a power plug. The RTC DS1307 Real Time Clock is used to set and retrieve the date/time of the chip. Serial clock and serial data of the RTC are connected to the analog pin 4 and 5 of Arduino respectively as default. Real time clock (RTC) and Arduino are connected as shown in Figure.3.

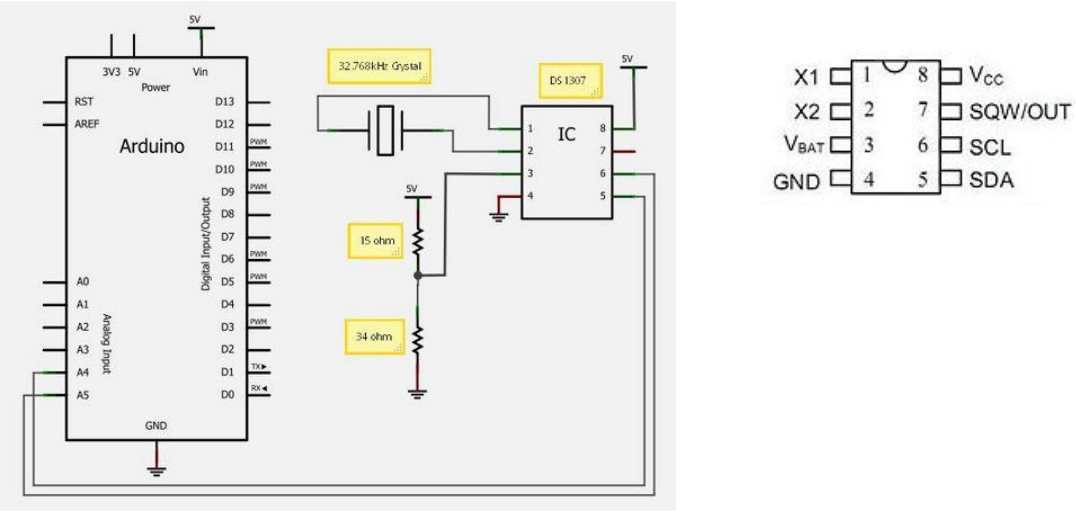

Figure.3 Connection of RTC with Arduino

Arduino Uno board

Arduino is an open source electronics prototyping platform based on flexible, easy-to-use hardware and software. It is intended for artists, designers, hobbyists and anyone interested in creating interactive objects or environments. Arduino Uno is based on ATmega328 microcontroller (MCU). It consists of 14 digital input/output pins, six analogue inputs, a USB connection for programming the onboard MCU, a power jack, an ICSP header and a reset button. It is operated with a 16MHz crystal oscillator and contains everything needed to support the MCU. It is very easy to use as you simply need to connect it to a computer using a USB cable, or power it with an AC-to-DC adaptor or battery to get started. The MCU onboard is programmed in Arduino programming language using Arduino IDE.

Operation

Circuit design

Temperature logger system consists of Arduino UNO R3, data logging shield, USB cable, microSD memory card. Pin1 (+5V), pin3 (ground) and pin 2 (data pin) of LM35 are connected to the 5V, Gnd and analog pin A0 of Arduino respectively. The serial clock (SCL) and the serial data (SDA) of the RTC 1307 are connected to the analog pin A5 and A4 respectively. Photograph of temperature logger circuit is shown in the Figure.4. Circuit connection is drawn in Fitzing software and it is illustrated in Figure.5.

Results and Discussion

The SD card logger, the real time clock (RTC), the temperature sensor LM35 are connected to the Arduino microcontroller. The temperature data will be displayed on the serial monitor for every prescribed time. But one can alter this time period by changing the value in delay. Simultaneously, these data are stored in the microSD card which is fitted to the SD card logger. The sketch and data stored on the serial monitor are illustrated in the Figure.6. The data on the serial monitor and the data stored in the SD card logger are shown in Figure.7 and Figure.8.

Conclusion

If the results don't appear in the Serial Monitor, then try the following until the problem is fixed:

(i) Make sure that the header sockets are soldered neatly and that the pins are not shorted out.
(ii) Check that the Serial Monitor baud rate is 57,600 and that a regular Arduino Uno–compatible board is being used. The Mega and some other board models have the SPI pins in different locations.

If the temperature has lack of precision with respect to the standard digital thermometer, this problem can be solved by removing the offset voltage in the sketch. In this research, 30mV is removed to obtain the precise temperature as shown in following part of sketch.

```
sensor = analogRead(0);
 voltage = (sensor*5000)/1024; // convert raw sensor value to millivolts
voltage = voltage-30        // remove voltage offset
 celsius = voltage/10;        // convert millivolts to Celsius
 fahrenheit = ((celsius * 1.8)+32);.
```

The removed offset voltage will be different for the different types of sensors.

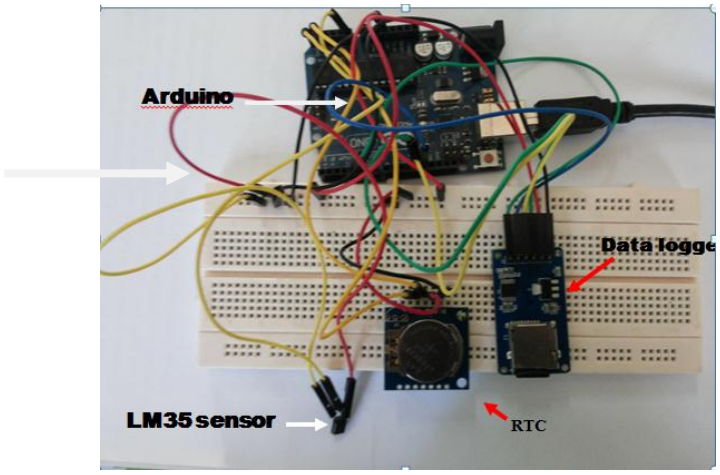

Figure.4 Circuit of data logger with real time

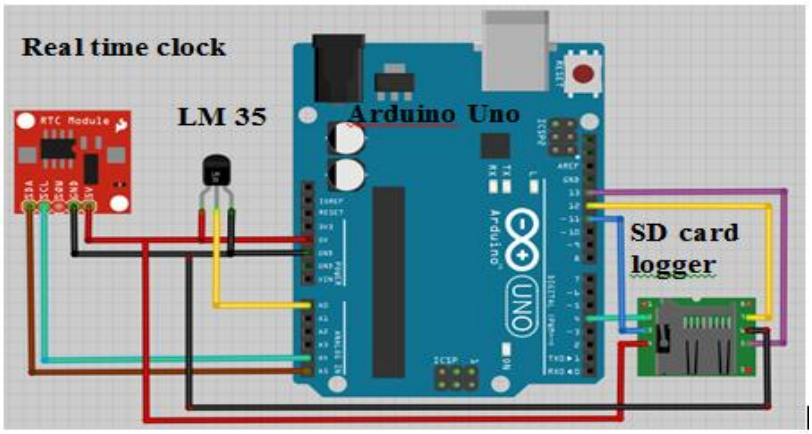

Figure.5 Data logger circuit drawn by Fritzing software

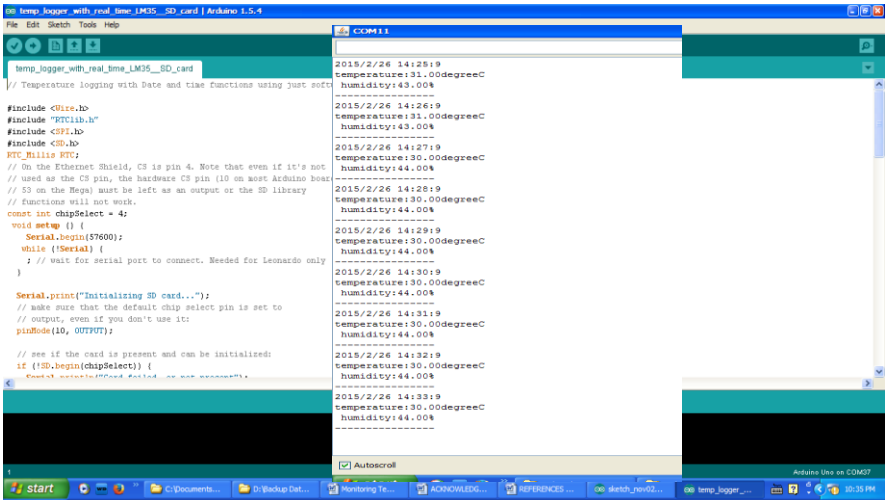

Figure.6 Sketch and data stored on the serial monitor

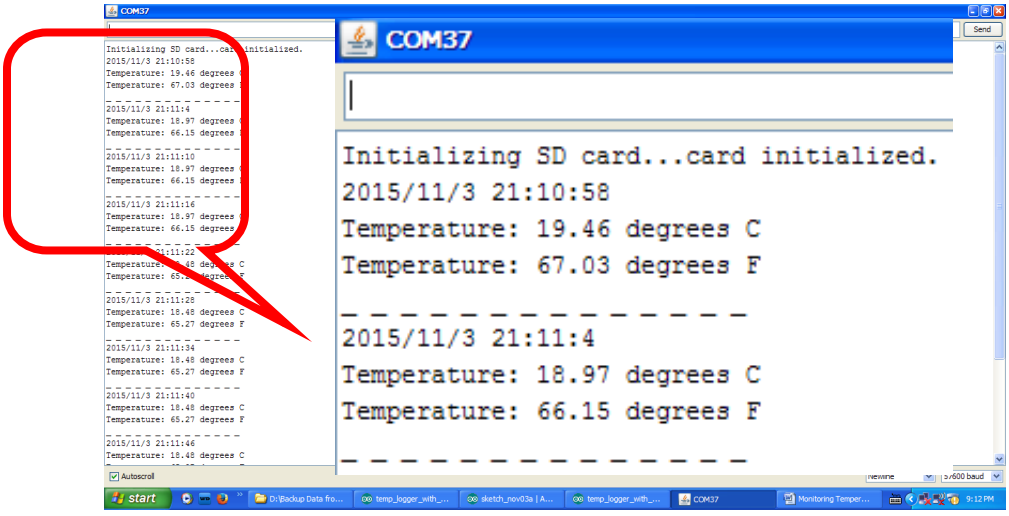

Figure.7 Data on the serial monitor

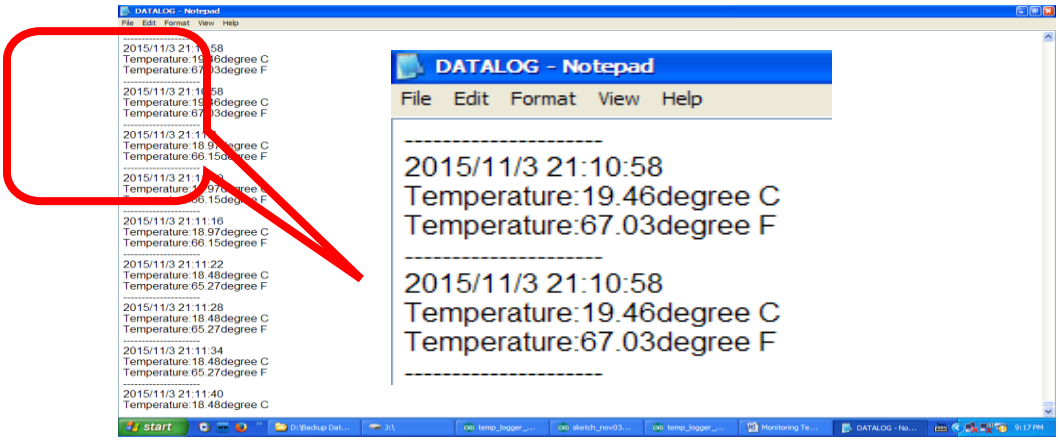

Figure.8 Data stored in SD card logger

Acknowledgements

I wish to express my sincere thanks to Dr Aung Kyaw Thin, Rector and Dr Aye Aye Han, Pro-Rector, Banmaw University for their permission to do this paper. I am very grateful to Professor Dr Than Than Lwin, Head of Department of Physics, Banmaw University for her kind permission to carry out this research.

References

Banzi M, 2009"Getting Started with Arduino" U.S.A.

Boxall J, 2013 " Arduino Workshop", No Starch Press, San Francisco.

A , 2013 "Android™ Open Accessory Programming with Arduino" , John Wiley & son inc.

Monk S, 2010"Arduino™ + Android™ Projects for the Evil Genius" Tab.

Monk S, 2010 "30 arduino projects for the evil geneius" Mc Graw-Hill Companies, Inc.

Coupled-Channels Calculations of Fusion Cross Sections and Fusion Barrier Distributions for ^{32,36}S + ^{90}Zr Systems

Aye Myat Wai[1], Ni Ni Yin[2], Tun Tun Naing[3], Hla Hla Win[4]

Abstract

The fusion cross sections and fusion barrier distributions of ^{32,36}S + ^{90}Zr systems have been calculated using Woods-Saxon nuclear potentials. Coupled-channels method and the code CCFULL are used in the calculations. The calculated results are compared with the experimental data. From the results, the information of the nuclei such as the types of coupling, multipolarity and number of phonons for the reactions can be obtained.

Keywords: fusion cross section, fusion barrier distribution, coupled-channels method

Introduction

Fusion is a process in which two colliding nuclei come close together to form a compound nucleus either by overcoming or by quantum tunneling through the potential barrier. We study in detail the fusion reaction of heavy elements at sub-barrier energies with coupled-channels method. This method approaches to investigate the large number of the degrees of freedom and a strong coupling between the projectile-target relative motion and the internal degrees of freedoms [1].The fusion cross section is the probability for the formation of a compound nucleus. It is determined experimentally by measuring the total rate of decay into the final products. The fusion cross section for the compound nucleus formation, σ_F, is obtained from the standard formula:

$$\sigma_F(E) = \frac{\pi}{k^2} \sum_l (2l+1)\, P_l(E), \qquad (1)$$

where $P_l(E)$ is barrier transmission probability or fusion probability of an angular momentum 'l'. In the study of fusion reactions, the important thing is how to precisely estimate the barrier transmission probability. The fusion barrier distribution is defined as the second derivative of the energy-weighted fusion cross sections with respect the centre-of-mass energy E, that is, $d^2(E\sigma_f)/dE^2$. The fusion barrier distribution has been shown tobe sensitive to the data related to the nuclear structure, such as the nuclear shapes, the multiple excitations and the nuclear surface vibrations, etc. The scope of this work is to investigate the fusion cross sections and the corresponding fusion barrier distributions by using Woods-Saxon potential in the interaction and also take into account the channel coupling effects. This is performed to decide the types of coupling, multipolarity and number of phonons for the reactions.

1 Dr, Lecturer, Department of Physics, Banmaw University
2 Dr, Lecturer, Department of Physics, Loikaw University
3 Dr, Lecturer, Department of Physics, Monywa University
4 Dr, Associate Professor, Department of Physics, Banmaw University

Coupled-Channels Method

The coupled-channels calculation is a standard theoretical approach to describe heavy-ion fusion reactions by taking the effects of nuclear intrinsic degrees of freedom into account. Therefore, we consider a collision between two nuclei in the presence of the coupling of the relative motion between the colliding nuclei $\mathbf{r} = (r, \hat{\mathbf{r}})$ to a nuclear intrinsic motion ξ. We assume the following Hamiltonian for the system

$$H(\mathbf{r}, \xi) = -\frac{\hbar^2}{2\mu}\nabla^2 + V(r) + H_0(\xi) + V_{coup}(\mathbf{r}, \xi). \qquad (2)$$

Here μ is the reduced mass of the system, V(r) is the bare potential in the absence of the coupling which consists of nuclear and Coulomb parts, $V(r) = V_N(r) + V_C(r)$, $H_0(\xi)$ is the Hamiltonian for the intrinsic motion and $V_{coup}(\mathbf{r}, \xi)$ is the coupling between them. The Schrödinger equation for the total wave function then reads

$$\left(-\frac{\hbar^2}{2\mu}\nabla^2 + V(r) + H_0(\xi) + V_{coup}(\mathbf{r}, \xi)\right)\Psi(\mathbf{r}, \xi) = E\,\Psi(\mathbf{r}, \xi). \qquad (3)$$

We expand the total wave function $\Psi(\mathbf{r}, \xi)$ with the eigen states of the intrinsic Hamitonian $H_0(\xi)$ as $\Psi(\mathbf{r}, \xi) = \sum_n u_n(r)\,\varphi_n(\xi)$, where $\varphi_n(\xi)$ satisfies $H_0(\xi)\varphi_n(\xi) = \varepsilon_n\varphi_n(\xi)$. The Schrödinger equation (3) for the total wave function can be transformed into a set of coupled equations

$$\left[-\frac{\hbar^2}{2\mu}\frac{d^2}{dr^2} + \frac{l(l+1)\hbar^2}{2\mu r^2} + V_N(r) + \frac{Z_p Z_T e^2}{r} - E + \varepsilon_n\right]u_n(r) + \sum_m V_{nm}(r)u_m(r) = 0 \qquad (4)$$

In general the internal degree of freedom ξ has a finite spin. We therefore expand the coupling Hamiltonian in multipoles

$$V_{coup}(\mathbf{r}, \xi) = \sum_{\lambda>0,\mu} f_\lambda(r)\,Y_{\lambda\mu}(\hat{\mathbf{r}})\cdot T_{\lambda\mu}(\xi). \qquad (5)$$

Here $Y_{\lambda\mu}(\hat{\mathbf{r}})$ are the spherical harmonics and $T_{\lambda\mu}(\xi)$ are the spherical tensors constructed from the internal coordinate. The full coupled-channels calculations quickly become very difficult to handle if many physical channels are included. The dimension of the resulting of coupled-channels problem is in general too large if several important intrinsic degrees of freedom exit simultaneously. For this reason, one often introduces the so called the no-Cariolis approximation to avoid these difficulties. In the no-Coriolis approximation to the coupled-channels equations, one first replaces the angular momentum of the relative motion in each channel by the total angular momentum J, that is

$$\frac{l(l+1)\hbar^2}{2\mu r^2} \approx \frac{J(J+1)\hbar^2}{2\mu r^2} \qquad (6)$$

This corresponds to the assumption that the change of the orbital angular momentum between the colliding nuclei due to the excitation of the intrinsic degree of freedom is negligible. Using $Y_{\lambda\mu}(\hat{\mathbf{r}} = 0) = \sqrt{(2\lambda+1)/4\pi}\;\delta_{\mu,0}$, the coupling Hamiltonian in the rotating frame becomes

$$V_{coup}(r,\xi) = \sum_{\lambda>0} \sqrt{\frac{2\lambda+1}{4\pi}}\, f_\lambda(r)\, T_{\lambda 0}(\xi). \qquad (7)$$

Since the coupling Hamiltonian does not depend anymore on the angular component of the relative coordinate between the colliding nuclei, the complicated angular momentum coupling vanish in the no-Coriolis approximation, and thus the coupled-channels equations are reduced. A remarkable fact is that the dimension of the coupled-channels equations is drastically reduced in the no-Coriolis approximation. In order to derive the coupled-channels equations in the no-Coriolis approximation, we expand the total wave function in the rotating frame as

$$\Psi(\mathbf{r},\xi) = \sum_{n\,I} \frac{u^J_{n\,I}(r)}{r}\, Y_{J0}(\hat{\mathbf{r}})\, \varphi_{n\,I\,0}(\xi) \qquad (8)$$

.

The radial wave function for the (nI)-th channel $u^J_{n\,I}$ is related to the original wave function as

$$u^J_{n\,I}(r) = \sum_{l} \langle I\,0\,J\,0 \,|\, l\,0\rangle\, u^J_{n\,l\,I}(r). \qquad (9)$$

The coupled-channels equations for $u^J_{n\,I}(r)$ then read

$$\left[-\frac{\hbar^2}{2\mu}\frac{d^2}{dr^2} + \frac{J(J+1)\hbar^2}{2\mu r^2} + V(r) - E + \varepsilon_{n\,I}\right] u^J_{n\,I}(r) + \sum_{n',\,I'\lambda>0} \sqrt{\frac{2\lambda+1}{4\pi}}\, f_\lambda(r) \left\langle \varphi_{n\,I} \middle| T_{\lambda\,0} \middle| \varphi_{n'\,I'} \right\rangle u^J_{n'\,I'}(r) = 0 \qquad (10)$$

In the case of heavy-ion fusion reaction, these coupled-channels equations are again solved by imposing the incoming wave boundary condition

$$u^J_{n\,I}(r) \sim T^J_{n\,I} \exp\left(-i \int_{r_{abs}}^{r} k_{n\,J\,I}(r')\, dr'\right),\ r \le r_{abs} \qquad (11)$$

$$= \left(H^{(-)}_J(k_{n\,I} r)\, \delta_{n,\,n_i}\, \delta_{I,\,I_i} + R^J_{nI}\, H^{(+)}_J(k_{n\,I} r)\right),\ r \to \infty \qquad (12)$$

Where $k_{n\,I} = \sqrt{\frac{2\mu}{\hbar^2}\left(E - \varepsilon_{nI}\right)}$ and the local wave number is defined by $k_{n\,J\,I}(r) = \sqrt{\frac{2\mu}{\hbar^2}\left(E - \varepsilon_{nI} - \frac{J(J+1)\hbar^2}{2\mu r^2} - V(r) - V^J_{n\,J\,I,\,n'\,J'\,I'}(r)\right)}$.

The transmission coefficients T^J_{nI} are obtained, the penetration probability through the Coulomb potential barrier is given by

$$P^J(E) = \sum_{n,\,I} \frac{k_{n\,J\,I}(r_{abs})}{k} \left| T^J_{n\,I} \right|^2. \qquad (13)$$

The fusion cross section is then given by

$$\sigma_F(E) = \frac{\pi}{k^2}\sum_J (2J+1)P^J(E) \qquad (14)$$

which is similar to equation (1) except that the penetrabilities $P^J(E)$ are influenced by the channel couplings.

Results and Discussion

We investigate the fusion cross sections and fusion barrier distributions by using coupled-channels method with Woods-Saxon nuclear potential for $^{32,36}S + {}^{90}Zr$ systems. The code CCFULL is used in the calculations. The potential parameters: the depth V_0, the radius R_0 and the diffuseness a used in the coupled-channels calculations are shown in Table 1. The low-lying excitations energies E^* and deformation parameters β_λ of targets and projectiles, $^{32,36}S$ and ^{90}Zr are shown in Table 2. The excitation energies E^* and the deformation parameters β_λ for all nuclei are taken from ref. [2, 3, 4].

(i) $^{32}S + {}^{90}Zr$ System

For the $^{32}S + {}^{90}Zr$ case, the coupling to the quadrupole vibration of the projectile ^{32}S and the quadrupole and octupole vibration of the target ^{90}Zr are included. For vibrational coupling, the coupling scheme is expressed as [P: $(n)^i$, T: $(n)^i$] for projectile and target where 'n' stands for type of polarity and 'i' for number of phonons. In this system, the couplings to the one-phonon [P: (2^+), T: (2^+), (3^-)] and two-phonon [P: $(2^+)^2$, T: $(2^+)^2$, $(3^-)^2$] states are taken into account. Figure (1) shows the results of the coupled-channels calculations of $^{32}S + {}^{90}Zr$ system for the fusion cross section (right panel) and the corresponding fusion barrier distribution (left panel), respectively. This figure compares the experimental data with the calculations without including the coupling effect, one phonon and two phonons couplings. The dotted line and solid line represent the results of the coupled-channels calculations including one phonon and two phonons states. The dashed line denotes the results in the absence of channel coupling. As shown in Figure (1), the calculations of fusion cross section in the absence of the channel coupling underestimate the experimental data at and below the Coulomb barrier. The calculations taking single phonon state and double phonon states enhance the fusion cross section to large extent as compared with the one dimensional barrier penetration model calculations. Coupling with single phonon state does not reproduce the pattern of the extracted experimental barrier distribution. We can see in Figure (1), the calculations with double phonon coupling reproduce the experimental data for the fusion cross section as well as the fusion barrier distribution.

(ii) $^{36}S + {}^{90}Zr$ System

We now discuss the heavy-ion fusion reaction of $^{36}S + {}^{90}Zr$ system. The coupled-channels calculations of fusion cross section as well as the fusion barrier distribution for this system are calculated by including the 2^+ (quadrupole) state of ^{36}S and the 2^+ (quadrupole) and 3^- (octupole) states of ^{90}Zr. The results of coupled-channels calculations are compared with the experimental data in Figure (2). In this figure, the right panel and the left panel show the fusion cross section and the fusion barrier distribution, respectively. The dashed line is the results of one dimensional model which fails to reproduce the experimental data of the fusion cross section as well as the fusion barrier distribution. We calculate the coupled-channels calculations by taking into account

the single quadrupole excitations of ^{36}S and single quadrupole and octupole excitations of ^{90}Zr [P: (2^+), T: (2^+), (3^-)]. The dotted line represents the results of calculations by taking single phonon coupling. The obtained fusion cross section underestimates the experimental data and the obtained fusion barrier distribution inconsistent with the experimental data. We then repeat the calculations by including the coupling up to the double phonon states of quadrupole excitations of the projectile and the double phonon states of quadrupole and octupole excitations of the target, ie., [P: $(2^+)^2$, T: $(2^+)^2$, $(3^-)^2$]. The solid line is obtained by taking into account the coupling up to double phonon states. It can be seen that the coupled-channels calculations with double phonon states agree the experimental fusion cross section and the corresponding fusion barrier distribution.

Table 1 The potential parameters V_0, R_0, *a* used in the coupled-channels calculations

System	V_0(MeV)	R_0(fm)	*a* (fm)
^{32}S+^{90}Zr	200.0	1.010	0.82
^{36}S+^{90}Zr	200.0	0.990	0.83

Table 2 The related information on the low-lying excitations energies and deformation parameters for different nuclei

Nucleus	λ^π	E^* (MeV)	β_λ
^{32}S	2^+	2.230	0.310
	3^-	5.006	0.400
^{36}S	2^+	3.291	0.160
	3^-	4.193	0.376
^{90}Zr	2^+	2.186	0.090
	3^-	2.748	0.220

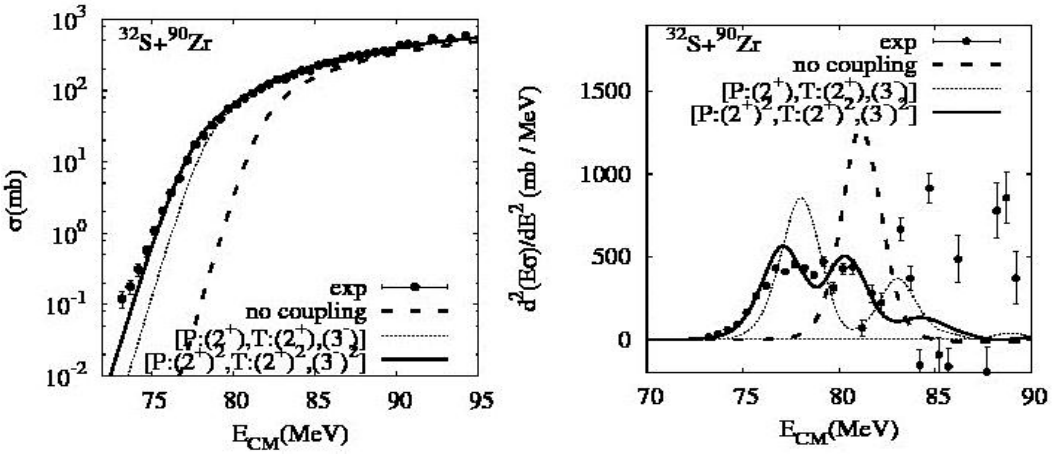

Figure (1) the fusion cross section (right panel) and the corresponding fusion barrier distribution (left panel)for ^{32}S + ^{90}Zr system. The experimental data are taken from [5].

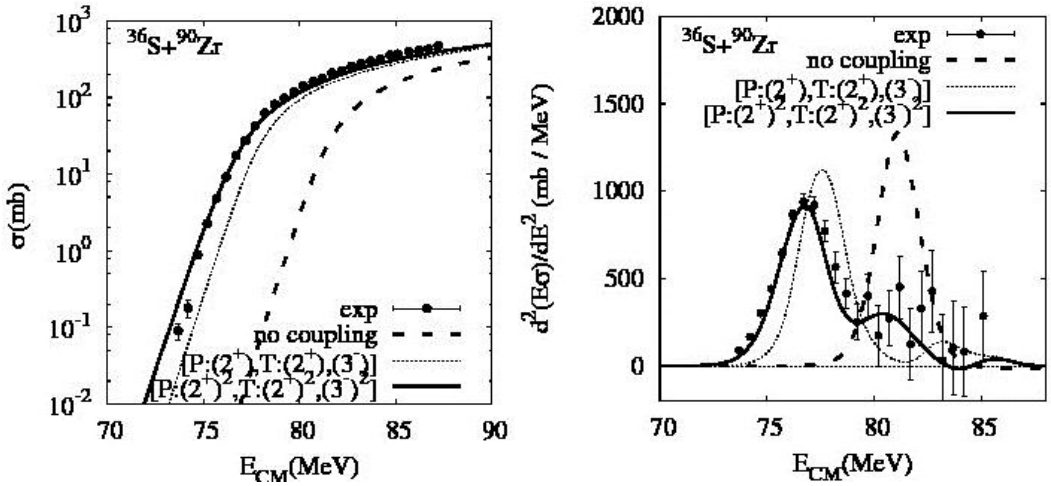

Figure (2) the fusion cross section (right panel) and the corresponding fusion barrier distribution (left panel) for ^{36}S + ^{90}Zr system. The experimental data are taken from [6].

Conclusion

We have performed the calculations of fusion cross sections and the corresponding fusion barrier distributions withcoupled-channels methodfor^{32,36}S + ^{90}Zr systems. From the results, we can get the information of the nuclei such as the types of coupling, multipolarity and number of phonons for the reactions. We can investigate the structure of heavy elements and get the information of the colliding nuclei from fusion cross sections and fusion barrier distributions. In fact, fusion barrier distribution is a powerful method to study the effects of the nuclear shape in heavy-ion nuclei.

Acknowledgement

I thank to Professor Dr Than Than Lwin, Head of Department of Physics, Banmaw University, for her encouragement and permission.

References

[1] K. Hagino, Ph.D. Thesis, Tohoku University (1998).

[2] http://nucleus.iaea.org/Pages/nu-dat-2.aspx.

[3] S. Raman, *et al*., At. Data Nucl. Data Tables **78** (2001) 1.

[4] T. Rumin, K. Hagino, and N. Takigawa, Phys. Rev. **C 61**(1999) 014605.

[5] H.Q. Zhang, *etal*., Phys. Rev. C **82** (2010) 54609.

[6] A.M. Stefanini, *et al*., Phys. Rev. C **62** (2000) 14601.

Investigation of Phase Formation and Structural Properties of $LiCo_{1-x}Ni_xO_2$

Lai Lai Win Hlaing[1], San San Htwe[2], Zin Zin Naing[3], Aye Myat Wai[4]

Abstract

A series of Nickel Doped Lithium Cobalt Oxide $LiCo_{1-x}Ni_xO_2$, (x = 0.00, 0.25, 0.50, 0.75, and 1.00) materials which are the Lithium-based transition metal oxides with layer structure were prepared with solid state reaction method. Stoichiometric ratios of Cobalt Oxide (CoO), Nickel Oxide (NiO) and Lithium Carbonate (Li_2CO_3) were used as starting metarials. The X-ray diffraction method and Fourier Transform Infrared (FTIR) spectroscopic method were used to identify the crystalline phase formation of the oxide particles. Morphological features of the samples were investigated by Scanning Electron Microscope (SEM). The X-ray diffraction patterns show that $LiCo_{1-x}Ni_xO_2$, has a well-developed hexagonal structure and the SEM analysis shows the particulate nature of the prepared materials with 2 µm to 5 µm.

Keywords: $LiCo_{1-x}Ni_xO_2$, solid state reaction method, crystalline phase formation and morphological features

Introduction

In these days, lithium based layered transition metal oxides have been carried out on doped $LiMO_2$ oxides (M = Ti, Cr, Mn, Ni, Fe, Cu, Co, Bi, Zn, Mo) which show interesting structural and electrochemical properties. These materials are important in the area of solid - state ionic, and are also known as solid electrolytes and superionic conductors. These materials possess high ionic conductivity which has numerous technological applications in a variety of solid state electrochemical devices such as solid-state batteries, super capacitors, electro-chromic displays, sensors, solid oxide fuel cell and electrochemical solar cells etc. Solid oxide fuel cells are a class of fuel cells characterized by the use of a solid oxide material as the electrolyte [*1*]. Solid electrolytes comprising lithium ionic conductor materials exhibit good safety and stability more than organic liquid electrolytes. The crystal structure of transition metal oxide involves in the family of layered oxides groups generally referred to as delafossite. Delafossite is a copper iron oxide mineral with formula $CuFeO_2$ or $Cu^{1+}Fe^{3+}O_2$.

Their crystal structures are isotypic, with the general chemical formula ABO_2 which is derived their name from the mineral $CuFeO_2$. Delafossite crystals typically have the chemical formula $A^{+1}B^{+3}O_2$. The structure group characterized by sheets of linearly coordinated A cations stacked between edge-shared octahedral layers (BO_6) is shown in Figure (1). In general, the unit cell of the crystal structure is characterized by layers of A-site cations planes that are alternatingly stacked with layers of edge-sharing octahedral having the B-site cations positioned in the center of each octahedron and oxygen anions at the corners of each octahedron [2]. Delafossite, along with other

1 Dr, Lecturer, Department of Physics, Banmaw University
2 Dr, Lecturer, Department of Physics, Banmaw University
3 Dr, Associate Professor, Department of Physics, Banmaw University
4 Dr, Lecturer, Department of Physics, Banmaw University

minerals of the ABO_2 group, is known for its wide range of electrical properties, its conductivity varying from insulating to metallic. Delafossite is usually a secondary mineral that crystallizes in association with oxidized copper and rarely occurs as a primary mineral.

The crystal structure of $LiCoO_2$ involves in the family of layered oxides groups generally referred to as delafossites. This research mainly focused on the effect of doping concentration of nickel in lithium cobalt oxide system and characterization of its structural properties. The investigations of structural properties were performed on the final sintering pellets for all Ni concentrations.

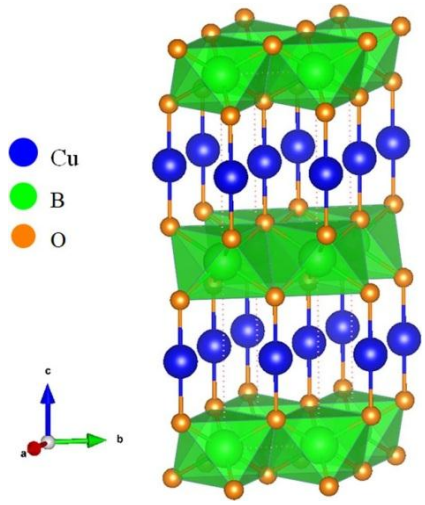

Figure (1) Crystal structure of Delafossite type [3]

Experimental

In the present work, high purity materials were used to prepare Nickel doped lithium cobalt oxide with the general formula $LiCo_{1-x}Ni_xO_2$, (x = 0.00, 0.25, 0.50, 0.75, 1.00) by using solid state reaction method. Firstly, lithium carbonate (Li_2CO_3), Cobalt Oxide (CoO) and Nickel Oxide (NiO) with desired stoichiometric compositions are used as starting materials as illustrated in Figure (2). These oxide materials were mixed with standard weight percentages according to their stoichiometric calculation by using the following equation.

$$Li_2CO_3 + 2(1–x)\ CoO + 2x(NiO) \longrightarrow 2\ LiCo_{1–x}Ni_xO_2 + CO$$

Firstly, the raw materials of Li_2CO_3, CoO and NiO were mixed and ground for 2 hours in an Agate mortar and then the mixed powders were pre-sintered at 450°C for 12 hours in electrical furnace.

After pre-sintering, the mixed powders were secondary ground by using Agate mortar for 3 hours to get very fine power. The powders were pressed into pellets by pellets maker machine. The oxide materials were final-sintered at 800°C for 3 hours. Finally, the final sintered pellets were formed as shown in Figure (3). The final-sintered samples had been analyzed by X-ray Diffraction Technique (XRD) and Scanning Electron Microscope (SEM) to identify the crystalline phase formation. The flow chart for preparation of nickel doped lithium cobalt oxide samples is shown in Figure (4). XRD measurement was carried out by using RIGAKU MINIFLEX 600 powder X-ray diffractometer at Department of Physics, Yangon University.

Figure (2) Photographs of starting materials which are prepared in the present work

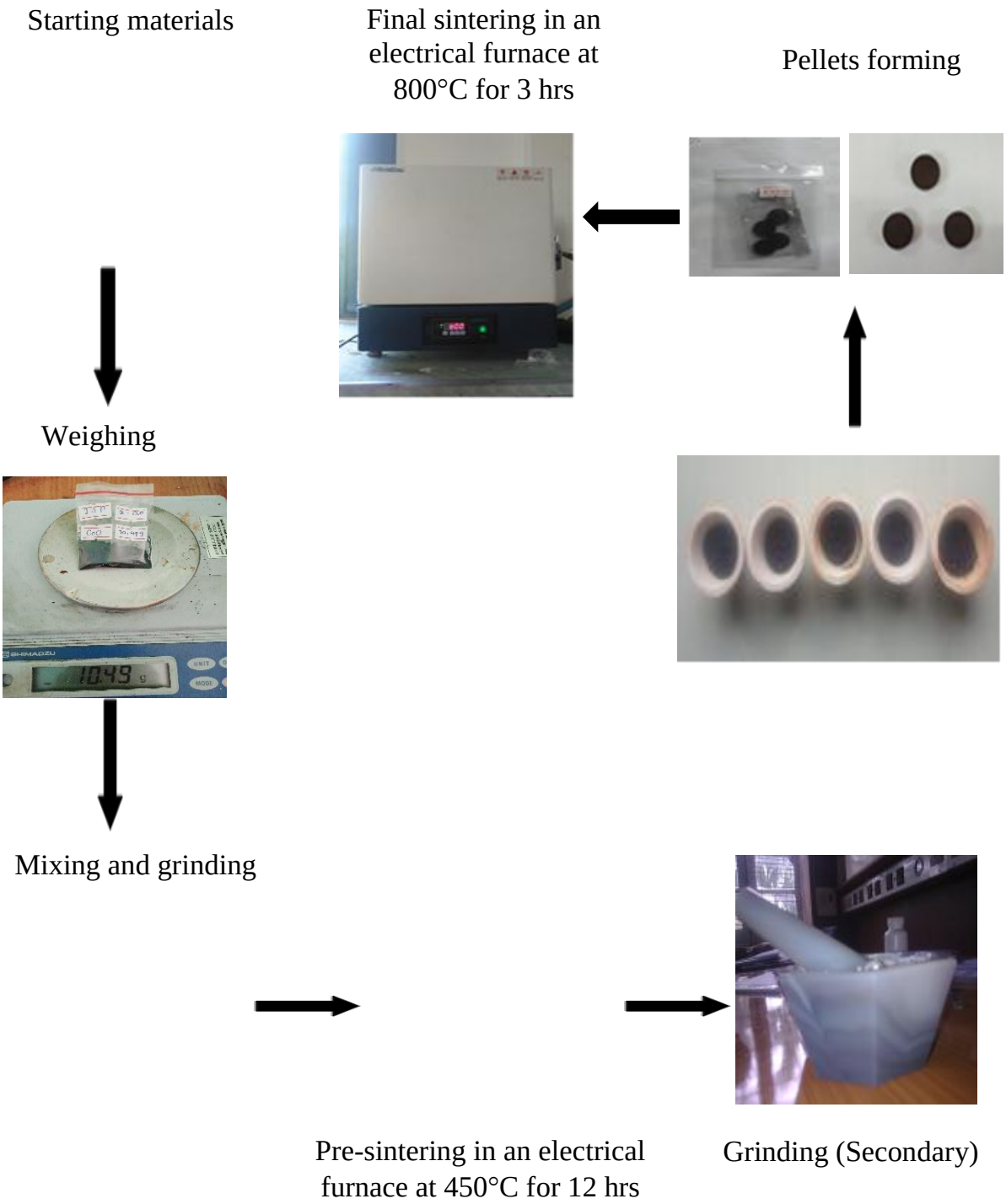

Figure (3) Photographs for preparation of $LiCo_{1-x}Ni_xO_2$ samples

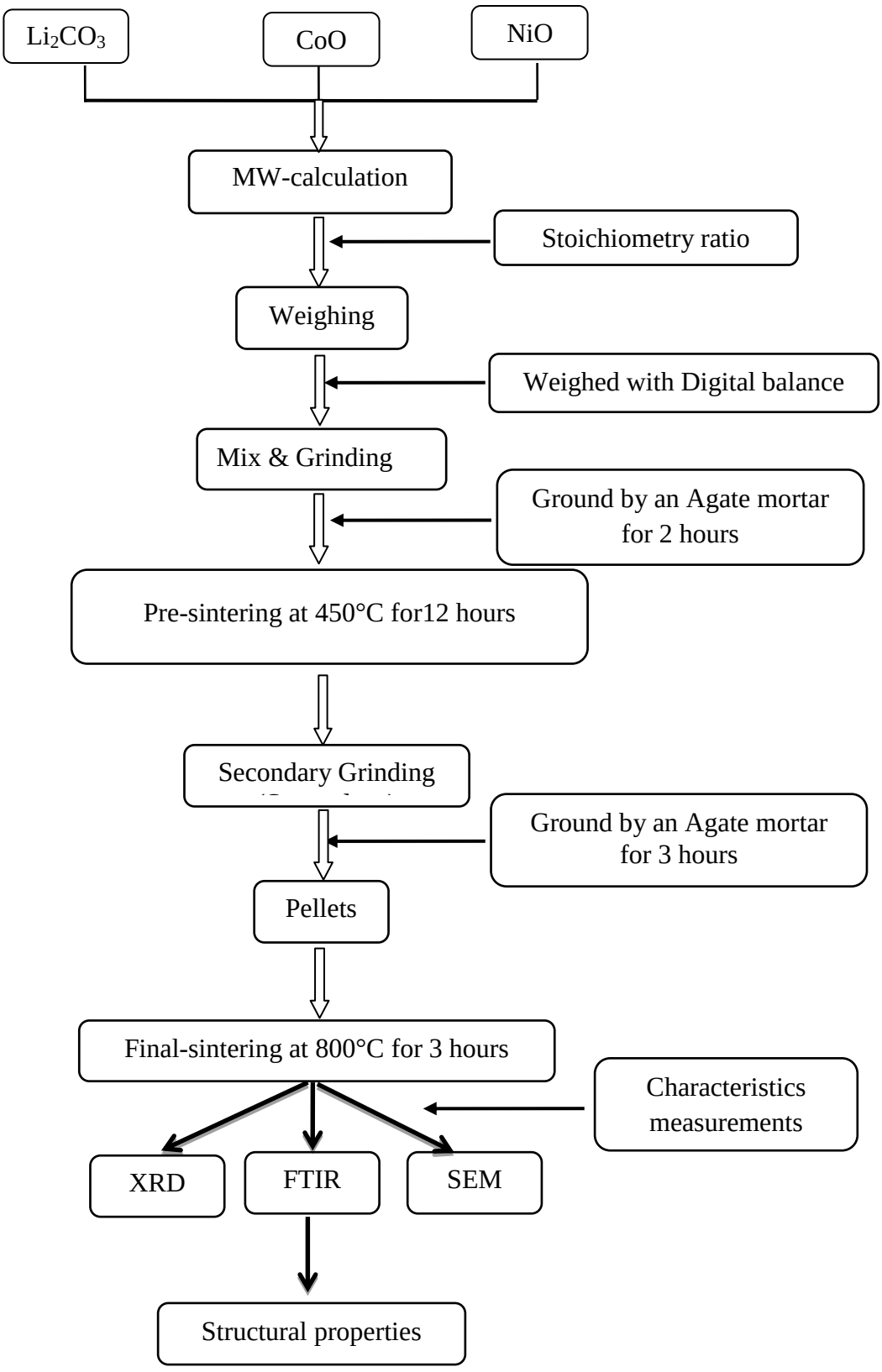

Figure (4) Flow chart for preparation of $LiCo_{1-x}Ni_xO_2$

Results and Discussion

(i) Phase analysis by XRD measurement

The XRD patterns of Nickel doped lithium cobalt oxide, $LiCo_{1-x}Ni_xO_2$, (x = 0.00, 0.25, 0.50, 0.75 and 1.00) are shown in Figure 5(a) to (e). All of the diffraction lines can be indexed with a hexagonal lattice. The observed XRD lines are identified by using ICDD (International data base) to assign the crystal planes (Miller indices) and to examine the crystal structure. The observed XRD spectrum of $LiCo_{1-x}Ni_xO_2$ for x = 0.00 is found to agree with ICDD data file of $LiCoO_2$ (Card. No. 00-062-0420). Here the sharp peaks indicate the good crystallinity. In the XRD patterns, (003) peaks indicates the property of layer structure of $LiCoO_2$, (104) peaks indicates the property of basic unit of Co-O-Co bond which form this kind of layer compound and the intensity ratio demonstrates the better crystallinity.

These figures reveal that all these materials are single phase with hexagonal symmetry, space group R3m. Figure 5(a) shows that the relative intensity ratio of (003) and (104) peaks in the $LiCoO_2$ is higher than in theoretical ratio 0.87 by assuming complete occupation of transition metals [4].The transition metal ions are in turn surrounded by six oxygen atoms. Infinite layers of $LiCo_{1-x}Ni_xO_2$ were formed through edge sharing of the ($LiCo_{1-x}Ni_xO_6$) octahedrals, with the intercalating lithium ions located between the layers. All of the diffraction lines can be indexed with a hexagonal lattice.

As the Co^{3+} ions at the 3a lattice sites of the $LiCoO_2$ lattice are partially replaced by Ni^{3+} ions, the unit cell dimensions, a and c, in a hexagonal setting become smaller. But it was found that the lattice parameter (c) becomes slightly increase with more than the critical condition of Ni doping concentration x=0.5.This result trend was agreed with the report of N.W.B. Balasooriya & P.W.S.K. Bandaranayake [5].

The lattice constants are found to be about 2.83 Å and 14.11 Å for x = 0.00, 2.33 Å and 14.06 Å for x = 0.25, 2.11 Å and 14.02 Å for x = 0.50, 2.17 Å and 14.12 Å for x = 0.75 and 2.67 Å and 14.16 Å for x = 1.00 respectively and consistent for all compositions. This decrease in lattice constants is due to the difference in ionic radii size between cobalt ion (0.82 Å) and nickel ions (0.76 Å). These results strongly suggest that $LiCo_{1-x}Ni_xO_2$ is in a homogenous phase, i.e. Ni^{3+} and Co^{3+} are homogenously located at the octahedral 3a sites in a cubic phased oxygen array.

The average crystallite sizes of the samples are listed in Table (1). The variation in crystallite sizes was investigated based on the amount of Ni ions doping. According to the observation of XRD data, it can be concluded that the crystallite size of the $LiCo_{1-x}Ni_xO_2$ samples decrease with an increase of Ni ions in $LiCoO_2$ system except more than the critical condition of Ni doping concentration x=0.5.

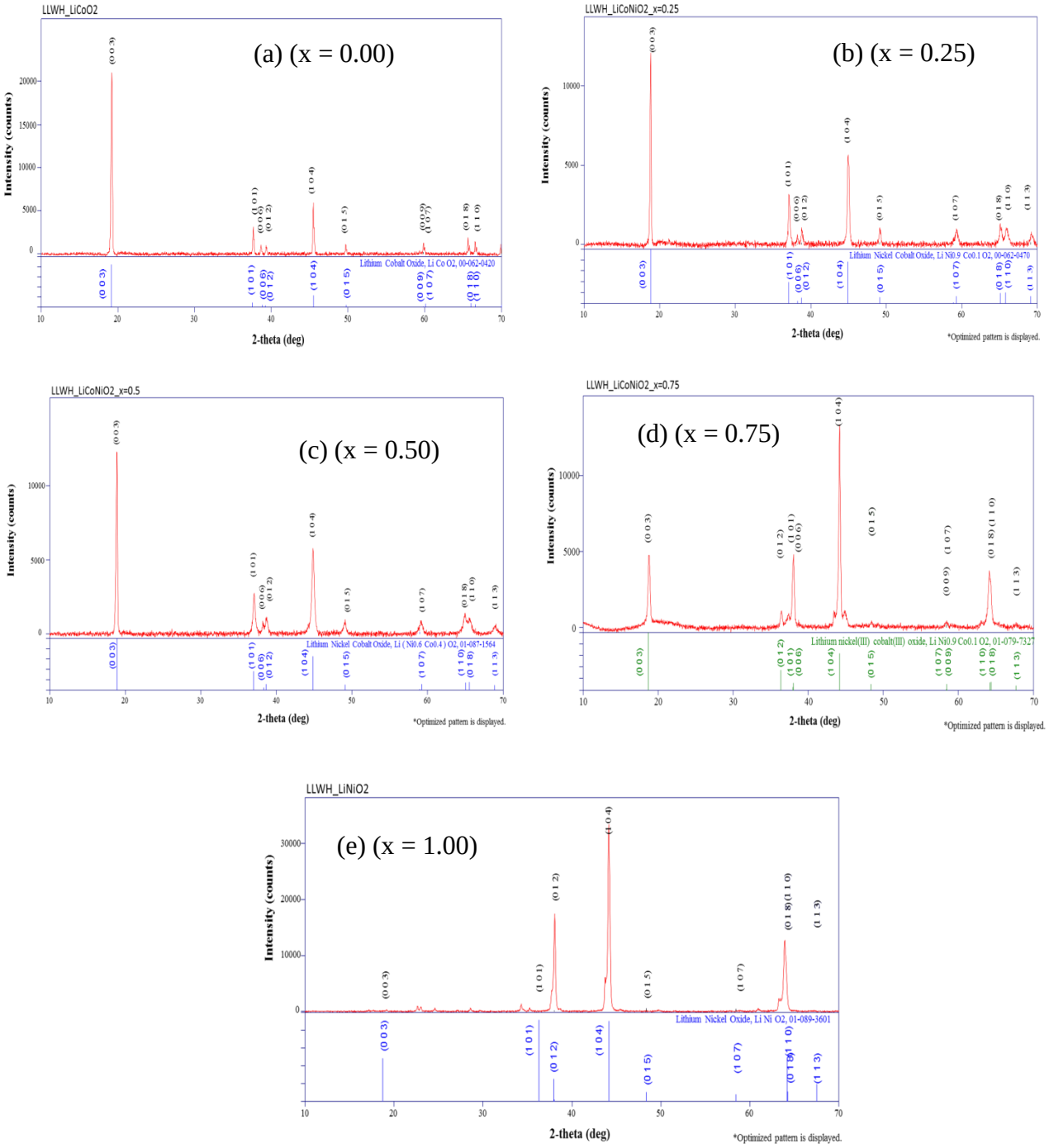

Figure 5 (a) to (e) XRD spectrums of $LiCo_{1-x}Ni_xO_2$ (where x = 0.00, 0.25, 0.5, 0.75 and 1.00)

Table (1) Comparison of crystallite sizes and lattice parameter of $LiCo_{1-x}Ni_xO_2$

x	Sample	Crystallize size (nm)	a (Å)	c (Å)
0.00	$LiCoO_2$	76.10	2.83	14.11
0.25	$LiCo_{0.75}Ni_{0.25}O_2$	36.17	2.33	14.06
0.50	$LiCo_{0.5}Ni_{0.5}O_2$	23.53	2.11	14.02
0.75	$LiCo_{0.25}Ni_{0.75}O_2$	38.33	2.17	14.12
1.00	$LiNiO_2$	41.04	2.67	14.16

(ii) Molecular vibrational analysis

The results of FTIR spectroscopic analysis are shown in the Figure 6 (a) to (f). FTIR measurements was made to investigate the local environment of cations in a cubic close-packed oxygen array of the $LiCo_{1-x}Ni_xO_2$ lattice. Infrared modes correspond to vibrations involving primarily atomic motion of oxygen anions against their cationic neighbors. It has been observed that $LiCoO_2$ contains the following transmssion bands: 609.53 cm^{-1}, 864.14 cm^{-1}, 1442.80 $cm^{-1}$and 3439.19 cm^{-1}. The band located around 600 cm^{-1} are attributed to the asymmetric stretching vibration of Co—O bond in CoO_6 elongated octahedra. The transmission peaks at 1442.80 cm^{-1} is due to the vibrations of the lithium cobaltite crystal lattice. The band observed in the wavenumber range around 3400 cm^{-1} represents the O—H stretching vibration of H_2O molecule due to KBr pellet technique.

In the Ni doping, the transmission peaks of NiO_6 octahedra can be observed at the wave number region around 1500 cm^{-1} - 1750 cm^{-1} . Upon Ni doping, it is observed that the peaks shift from 609.53 cm^{-1} for (x= 0.00) to 592 cm^{-1} for (x=0.25) of Ni concentration, 574 cm^{-1} for (x=0.5) and 563 cm^{-1} (for x=0.75). This result shows that the shift of the band position of the CoO_6 vibrations is due to the increase of the electronic conductivity in Ni-rich samples. In (x=1) of Ni concentration sample, the strongest vibration mode of NiO_6 is observed at 1518 cm^{-1} due to an asymmetric stretching mode of the NiO_6 octahedra and the cobalt vibration mode which is around 500 cm^{-1} - 600 cm^{-1} is disappeared because of no cobalt concentration.

According to Fourier Transform Infrared (FTIR) spectroscopic method, the vibrational peaks were assigned with their specific wave numbers. The peaks shift has found to the lower wave number region upon Ni doping due to the increase of the electronic conductivity in Ni-rich samples [6]. It can be concluded that the molecular vibration of the respective molecules could confirmed the formation of $LiCo_{1-x}Ni_xO_2$ in this research.

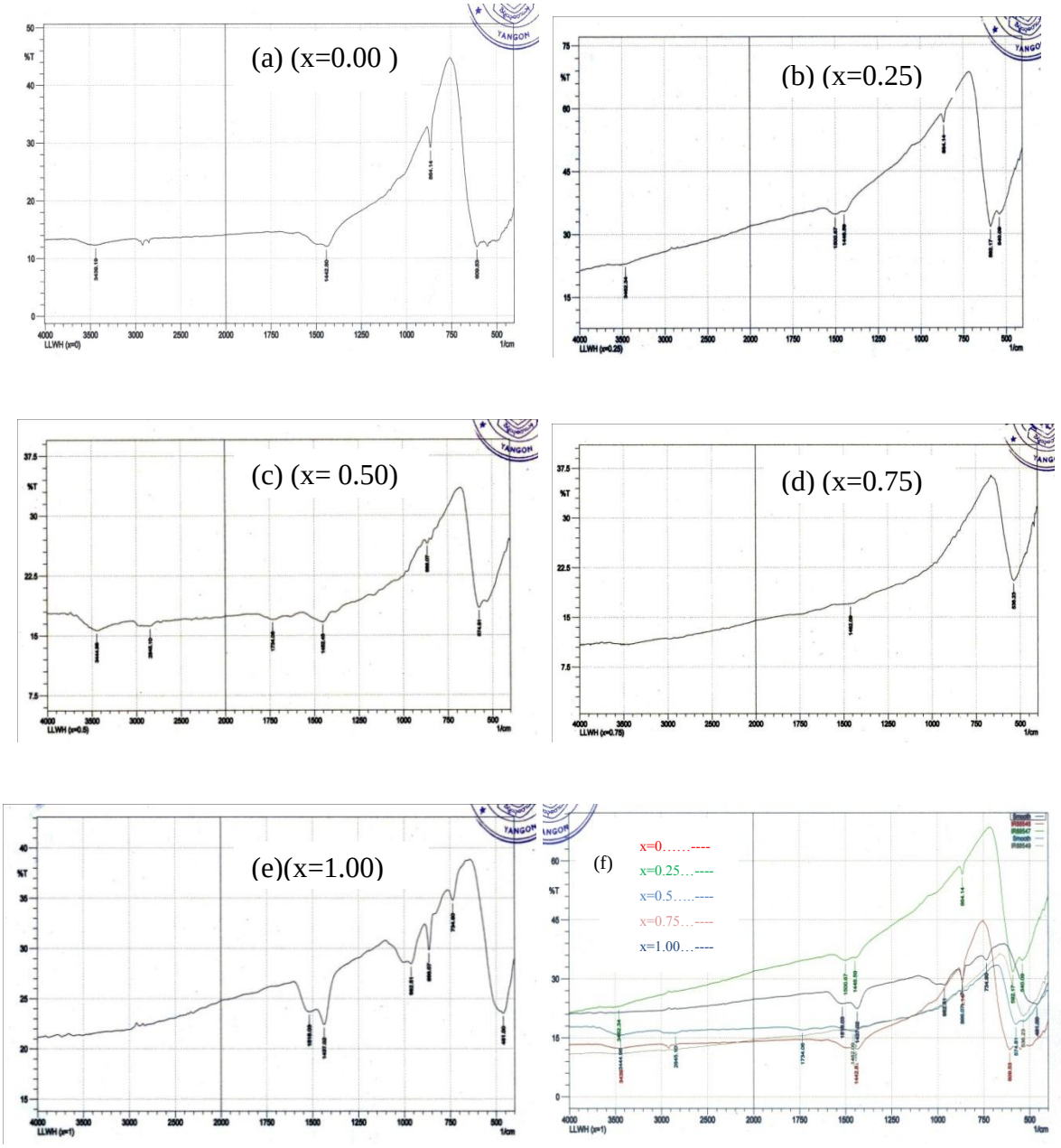

Figure 6 (a) to (f) FTIR spectra of $LiCo_{1-x}Ni_xO_2$ (x= 0.00 to1.00)

(iii) Microstructural analysis

The surface morphological features of synthesized particles were studied by scanning electron microscope. The SEM photographs of $LiCo_{1-x}Ni_xO_2$ final-sintered pellet at 800 ºC for 3 hrs were shown from Figure 7(a) to (e) with magnification of 2000 times. The SEM pictures indicated that the size of polycrystalline particles. The particles are found to be well-defined facets that have a wide range of distribution ranging from 2 µm to 5µm. The pristine $LiCoO_2$ sample contains bundle of agglomerated particles and relatively small particles on the agglomerates.

Surface morphology reveals that the average grain size decreases with an increase of Ni doping contents in $LiCoO_2$. But it was found that the grain size becomes slightly increase with more than the critical condition of Ni doping concentration x=0.5. The average grain size was estimated as shown in Table (2). The electrochemical properties of solid electrolyte materials mainly depend on the structure and morphology of the materials characteristic to different synthesis methods.

Table (2) Comparison of average grain size of $LiCo_{1-x}Ni_xO_2$ pellets

Ni Composition (x)	**Sample**	**Grain Size (μm)**
0.00	$LiCoO_2$	5.02
0.25	$LiCo_{0.75}Ni_{0.25}O_2$	3.08
0.50	$LiCo_{0.5}Ni_{0.5}O_2$	2.02
0.75	$LiCo_{0.25}Ni_{0.75}O_2$	2.23
1.00	$LiNiO_2$	2.99

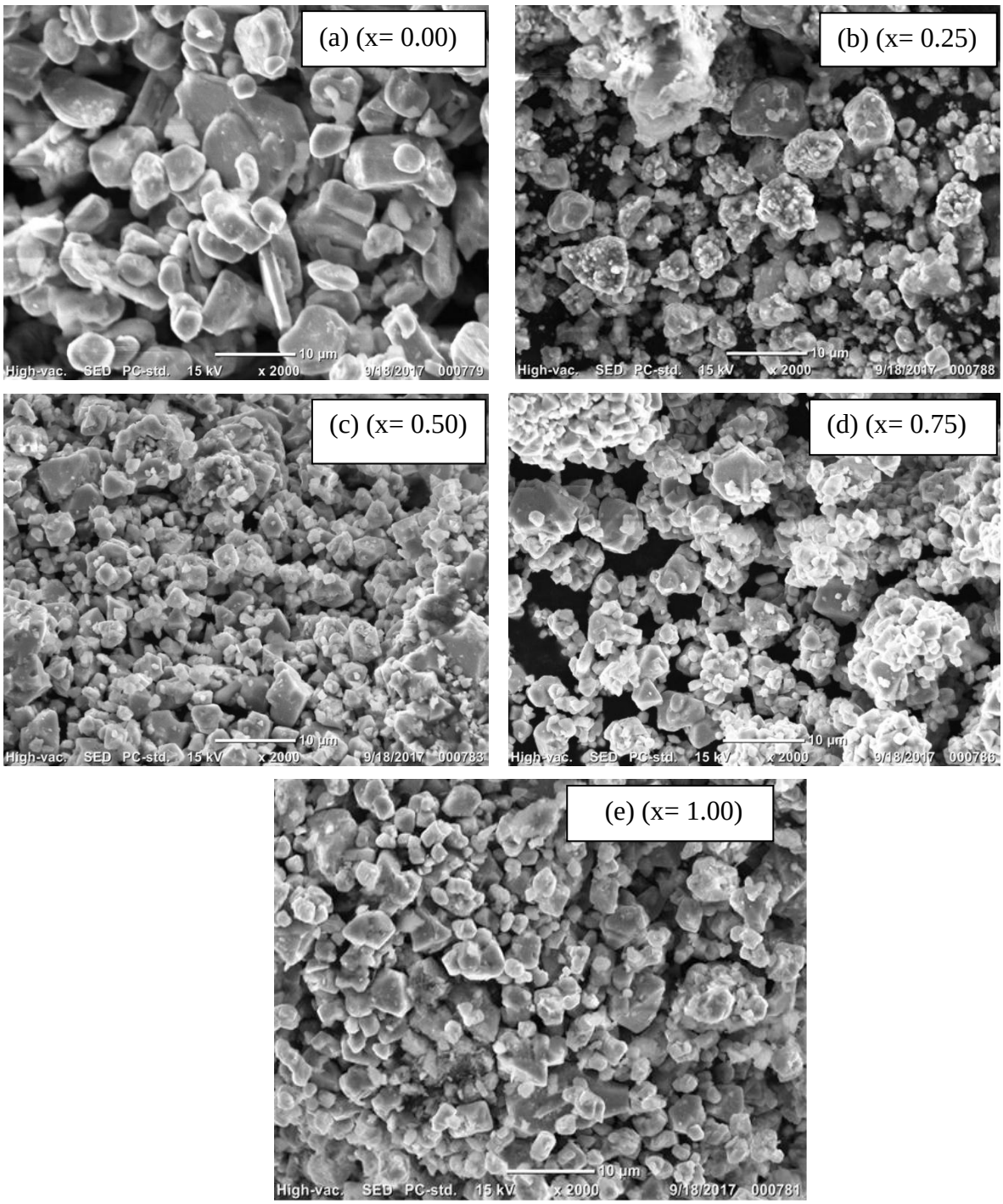

Figure 7 (a) to (e) SEM photos of $LiCo_{1-x}Ni_xO_2$ (where x = 0.00, 0.25, 0.50, 0.75 and 1.00)

Conclusion

According to the observation of XRD data, it can be concluded that the crystallite size of the $LiCo_{1-x}Ni_xO_2$ sample decreases with an increase of Ni ions in $LiCoO_2$ system except more than the critical condition of Ni doping concentration x=0.5. According to Fourier Transform Infrared (FTIR) spectroscopic method, the peaks shift has found to the lower wave number region upon Ni doping due to the increase of the electronic conductivity in Ni-rich samples. It can be concluded that the molecular vibration of the respective molecules could confirmed the phase formation of $LiCo_{1-x}Ni_xO_2$ in this research. Surface morphology revealed that the particle size decreases with the increase of Ni doping content in $LiCoO_2$. But it was found that the grain size becomes slightly increase with except more than the critical condition of Ni doping concentration x=0.5. Therefore $LiCo_{1-x}Ni_xO_2$ sample could successfully prepared by solid state reaction method and it has hexagonal structure. Finally it can be concluded that the doping of x=0.50 amount of nickel in lithium cobalt oxide ($LiCoO_2$) system exhibits the critical condition and more effective for the applications of a variety of solid state electrochemical devices.

Acknowledgement

I thank to Professor Dr Than Than Lwin, Head of Department of Physics, Banmaw University, for her encouragement and permission.

References

[1] R. Kanno & M. Murayama. (2001). "Lithium ionic conductor thio-LISICON. The Li_2S-GeS_2-P_2S_5 system", J. Electrochem. Soc., 148 (7), A742-A746.

[2] A.R. West. (2003). "Solid State Chemistry and its applications", John Wiley & Sons Pt. Ltd., Singapore.

[3] Anthony, W. John, Bideaux & A. Richard . (1997). "Delafossite"; Handbook of Mineralogy, Mineralogical Society of America.

[4] T. Haisheng, Z. Feng, H. Liu, X. Kan & P. Chen. (2011). "Reality and Future of Rechargeable Lithium Batteries". The Open Materials Science Journal, 5. (Suppl 1 : M 2) 204-214.

[5] N.W.B. Balasooriya & P.W.S.K. Bandaranayake, (2007)."Electrochemical Properties of $LiCo_{0.4}Ni_{0.6}O_2$ and its Performances in Rechargeable Lithium Batteries". Peradeniya. Sri Lankan Journal of Physics, Vol. 8 , 47-58.

[6] F. Gendron , S. Castro-Garciab, E. Popovac, , S. Ziolkiewicza, F. Soulettea & C. Juliena. (2003). "Magnetic and electronic properties of lithium cobalt oxide substituted by nickel" Proceedings of the 6th International Symposium on Systems with Fast Ionic Transport (ISSFIT), Volume 157, Issues 1–4, Pages 125–132.

Study On Gamow-Teller Transition Strengths In Beta Decay of ^{24}Al

San San Htwe[1], Khin Myo Chit[2], Lai Lai Win Hlaing[3], Kalayar Win[4]

Abstract

The Gamow-Teller transitions of ^{24}Al through nuclear beta-decay were studied. The beta-decay processes are also investigated. The beta-decay probability of the nucleus is calculated using time-dependent perturbation theory. The relation between the beta-decay probability and the comparative half-life of beta emitter were derived. By using this relation, the transition strengths of ^{24}Si, beta-plus (β^+) decay of ^{24}Al, are calculated. Finally, our results were compared with those from other research paper.

Keywords: beta-decay, Gamow-Teller (GT) transition strengths

Introduction

A nucleus with an abundance of neutrons or protons can transform to a more stable nucleus by emitting an electron or a positron. This kind of process is known as beta decay. The electron or positron (electron with positive electric charge, or antielectron) is called beta particle. There are three types of beta decay namely beta-minus (β^-) decay, beta-plus (β^+) decay and electron capture process. The nuclear beta-decay can be classified by the angular momentum carried away by the electron and neutrino. The most important are those with zero orbital angular momentum which are referred to as allowed beta decay. Angular momentum must be conserved during the transition between the initial and final states in the beta decay process leading to a restrictive set of selection rules. If the beta particle and neutrino are emitted with zero orbital angular momentum, $\ell = 0$, then only the intrinsic spins of the beta particle and neutrino need to be considered in the transition between initial and final states. The transitions with $\Delta\ell = 0$ are referred to as allowed beta decays.

There are two types of allowed beta decay namely Fermi (F) and Gamow-Teller (GT) transitions. We know that both the beta particle and neutrino have an intrinsic spin $s = \frac{1}{2}$. If the spin of the β particle and neutrino are anti-parallel (s = 0), the total change in nuclear spin, ΔJ, between initial and final states must be zero and the beta decay is termed as Fermi decay. If the electron and neutrino are emitted with their spins aligned (s = 1), then $\Delta J = 0$, ±1and the beta decay is called Gamow-Teller decay. The weak interaction in beta -decay plays a critical role in the initial step of the hydrogen fusion reaction leading to nucleosynthesis, and in the electron capture reactions leading to stellar collapse and supernova formation. The allowed β- decay can provide the most direct information on the Gamow Teller transition strength B(GT). The strengths of GT transitions, B(GT), are important physical quantities in understanding nuclear structures.

1 Dr, Lecturer, Department of Physics, Banmaw University
2 Dr, Lecturer, Department of Physics, Yadanabon University
3 Dr, Lecturer, Department of Physics, Banmaw University
4 Dr, Lecturer, Department of Physics, Pakokku University

B(GT$_+$) Evaluation from β-Decay Data

In order to evaluate B(GT$_+$) strength from beta-decay data, we have to use the half-life, branching ratio and the end point energy of an allowed β-transition related to the corresponding nuclear transition matrix element. The ft value is defined as the product of the partial half-life and the integrated Fermi function. The partial half-life was deduced using the half-life and the branching ratio. According to the equation $\frac{d\sigma}{d\Omega} = \frac{M_i M_f K_f}{4\pi^2\hbar^4 K_i}|B_{fi}|^2$, the connection between β-decay rate and Fermi or Gamow-Teller matrix element between initial and final nuclear states may be written as

$$\frac{\ln 2}{ft_{\frac{1}{2}}} = \frac{1}{K_0}\left(g_V^2 B(F_{\pm}) + g_A^2 B(GT_{\pm})\right) \quad (1)$$

where, g_V and g_A are vector and axial vector coupling constant respectively. Then we get

$$\frac{K_0 \ln 2}{g_V^2 ft_{\frac{1}{2}}} = B(F_{\pm}) + \frac{g_A^2}{g_V^2} B(GT_{\pm}) \quad (2)$$

Letting the constant $c=\frac{K_0 \ln 2}{g_V^2}$, the equation (2) becomes

$$\frac{c}{ft_{\frac{1}{2}}} = B(F_{\pm}) + \frac{g_A^2}{g_V^2} B(GT_{\pm}) \quad (3)$$

In order to evaluate the B(GT$_+$) strength of ^{24}Si β$^+$-decay, we consider the transition from the ground state of ^{24}Si to the first excited state of ^{24}Al. For pure Fermi transition, $(\text{i.e } 0^+ \rightarrow 0^+)$, the Gamow-teller transition strength is zero and the equation (3) reduces to

$$\frac{c}{ft_{\frac{1}{2}}} = B(F_{\pm}). \quad (4)$$

For a transition between analogous states (T=1) , the value of $B(F_{\pm})$ is 4. Therefore, the above equation (4) becomes

$$c = 4ft_{\frac{1}{2}} \quad (5)$$

By using the equation (5), we can get the value of constant c which is nearly equal to 6145 ± 4. For a Gamow-teller transition such as $(0^+ \rightarrow 1^+)$, the Fermi strength $B(F_{\pm})$ is zero and the equation (3) reaches the following equation,

$$\frac{c}{ft_{\frac{1}{2}}} = \frac{g_A^2}{g_V^2} B(GT_{\pm}) \quad (6)$$

If we substitute the value of c in equation (6), we then get the equation (7),

$$\frac{g_A^2}{g_V^2} B(GT_{\pm}) = \frac{6145\pm4}{ft_{\frac{1}{2}}} \quad (7)$$

The Q_{EC} value of the β$^+$-decay in ^{24}Si is 10.812 MeV and the half-life is 0.14 ± 0.08 s. The half-life for a particular final state can be obtained from the following relation

$$t_{\frac{1}{2}} = \frac{T_{\frac{1}{2}}}{b}, \quad (8)$$

where, $T_{\frac{1}{2}}$ is the total half-life of β-decay and b is the branching ratio of excited state in ^{24}Al. The transition strengths of the ^{24}Si β^+-decay can be calculated by using the equation (7) and the ratio $\frac{g_A}{g_V} = -1.266 \pm 0.004$ .The β-decay spectroscopy has an advantage for spin-parity assignment in term of log (ft).

Results and Discussion

The excitation energy, the branching ratio and the partial half-life for each particular final state were described in Table (1) and the Gamow-Teller$(GT)_+$ transitions of ^{24}Al from T_z = -2 to T_z = -1 were studied by β^+ decay as shown in Figure (1). As shown in Table (2), we found seven pairs of corresponding Gamow-Teller transition states at excitation energies E_x below 5.0 MeV in ^{24}Al and compared research paper respectively. The J^π values for the first five pairs at $E_x \leq 4.389$ MeV are consistent. This suggests that they are isobaric analogous states. The transition strengths B(GT) values of these first four pairs obtained from our calculation also agree with those from ^{24}Mg (^{3}He, t) ^{24}Al reaction except for the states above 5MeV in ^{24}Al. The J^π values for the next energy states in ^{24}Al are also consistent. Although the energy states are relatively similar, the B(GT) values of these states are quite different. This is because although we assume the nuclear interactions are charged independent, the Coulomb force in real nuclei may break isospin symmetry. Both the excitation energies and the B(GT) values are similar and consistent for the all state in ^{24}Al and the J^π values for these states are consistent. Although the excitation energies of the last two energy states are slightly different, the B(GT) strengths are also.

Table (1) The Excitation Energy, the Branching Ratio, The ft-value and B(GT) Strength of the beta decay of ^{24}Al

No	Excitation Energy in (MeV)	Branching ratio (%)	Parent ^{24}Si (J^+)	Daughter ^{24}Al (J^+)	Partial half-life (s)	B(GT_+) strength
1	0.426	31	0^+	1^+	0.45	0.124
2	1.090	23.9	0^+	1^+	0.59	0.136
3	2.991	5.78	0^+	1^+	2.42	0.134
4	3.364	11.09	0^+	1^+	1.26	0.334
5	4.389	1.00	0^+	1^+	14.00	0.033
6	4.670	1.39	0^+	1^+	10.07	0.099
7	4.970	1.31	0^+	1^+	10.69	0.092

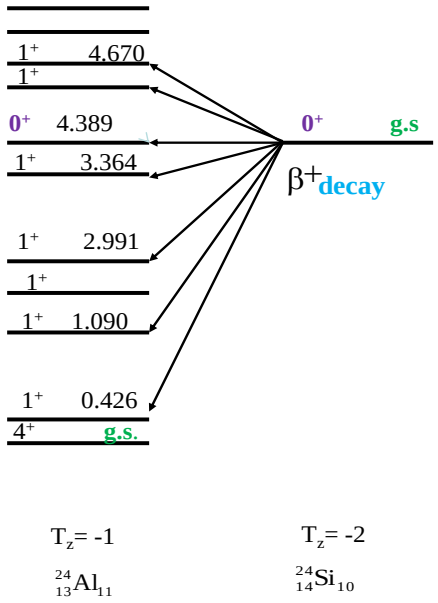

Figure (1) Level scheme of A=24 nuclei. The GT_+ transitions from $T_z = -2$ to $T_z = -1$ were studied by β^+ decay. The excitation energy is in MeV unit.

Table(2) The comparison of the excitation energies, J^π values and the transition strengths B(GT) obtained from the beta decay of ^{24}Si and other compared paper

No.	Excitation Energy in (MeV)	^{24}Al	B(GT) strength	Excitation Energy in (MeV)	^{24}Al	B(GT) strength
1.	0.426	1^+	0.124	0.426	1^+	0.13
2.	1.090	1^+	0.136	1.090	1^+	0.14
3.	2.991	1^+	0.134	2.991	1^+	0.14
4.	3.364	1^+	0.334	3.364	1^+	0.34
5.	4.389	1^+	0.033	4.389	1^+	0.03
6.	4.670	1^+	0.099	4.700	1^+	0.10
7	4.970	1^+	0.092	4.976	1^+	0.10

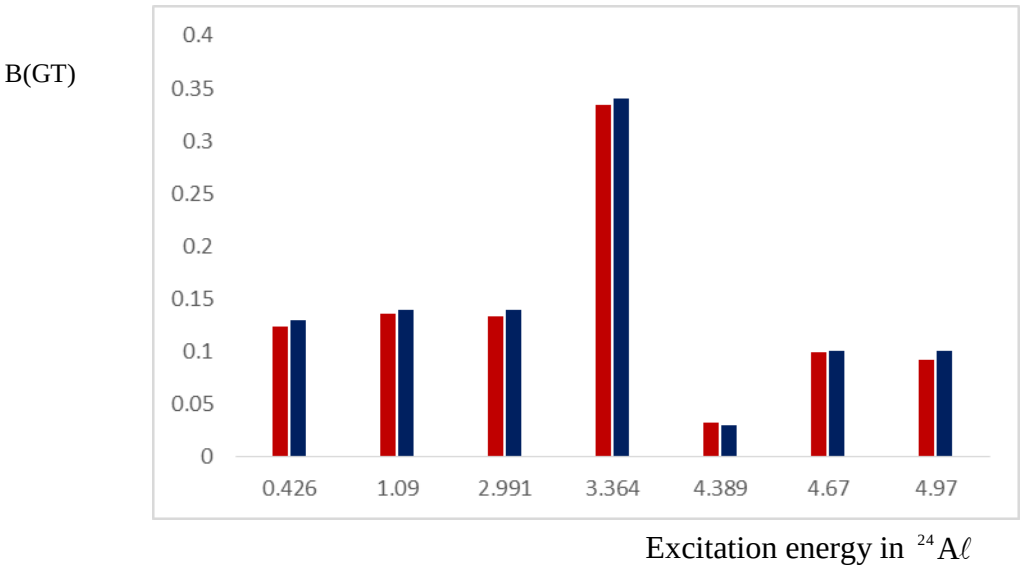

Fig. (2) B(GT) distribution from beta decay of ^{24}Si and compared paper

Conclusion

It is found that the energy difference of the corresponding states in ^{24}Al is at most 4.670MeV. The J^{π} values of most of the corresponding states are also consistent. But the B(GT) values of the corresponding states in ^{24}Al are quite different. Therefore, isospin symmetry in terms of the excitation energy and J^{π} value is rather good.

Acknowledgement

I deeply thank to Professor Dr Than Than Lwin, Head of Department of Physics, Banmaw University, for her encouragement and kind permission.

References

F. Osterfeld, Rev. Mod. Phys, **64** (1992) 491.

Y. Fujita *et al*., Phys. Rev. C **67** (2003) 064312.

H.A. Enge "Introduction to Nuclear Physics", Addison-Wesley Publishing Co Ltd., U.S.A (1974).

K. Schreckenbach *et al.*, Phys. Lett. **B 349** (1995) 427.

www.nndc.bnl.gov › nudat2.

R.G.T. Zegers *et al.*, Phys. Rev. **C 78** (2013).

A. Bohr and B.R. Mottelson, "Nuclear Structure", vol. **2**, Benjamin, New York (1975).

Y.Ichiawa, PhysRevC.80.044302